

# Stability Analysis of Space Debris Towing Systems

Anjali Jindal, Department of Mechanical Engineering

McGill University, Montreal

December 2023

Supervised by Professor Arun Misra

A thesis submitted to McGill University in partial fulfillment of the  
requirements of the

Undergraduate Honours Program in Mechanical Engineering

©Anjali Jindal, 2023

# Abstract

Active space debris removal using a tug is a promising technique for removing space debris. These systems consist of a space tug attached to orbiting debris via a thin tether and benefit from being cost-effective, applicable to a variety of debris shapes and sizes, and technologically ready for implementation. Unfortunately, the dynamics of the tug-tether-debris system is highly nonlinear and is susceptible to unstable or even chaotic oscillations. In this work, the stability of space debris towing systems is studied considering aerodynamic drag in Low Earth Orbit. The equations of motion are derived using the Lagrangian method in the reference frame of the space tug where motion is confined to the two-dimensional orbital plane and the space tug has a prescribed orbital motion. Numerical simulation is conducted for a variety of cases to study the behaviour of equilibrium points, tether oscillations, and stabilization methods. The key parameters of interest are the aerodynamic properties of the debris, the orientation of the tether, and the effects of magnitude and direction of thrust applied to the spacecraft. These methods explore the effect of aerodynamics on tethered satellite systems which remains understudied. Furthermore, modeling the system in the frame of the space tug as opposed to the centre of mass of the system facilitates the use of these findings in control system design as this location can be more easily tracked. Understanding the behaviour and dynamics of the system in these terms is key to the design of space-debris removal systems, control systems, mission design and end-of-life satellite design.

# Abrégé

L'élimination des débris spatiaux à l'aide d'un remorqueur est une technique prometteuse pour éliminer les débris spatiaux. Ces systèmes sont constitués d'un engin spatial attaché aux débris en orbite via un ancrage et bénéficient d'un bas coût, d'être applicables à une variété de formes et de tailles de débris et prêts technologiquement à être mis en œuvre. Malheureusement, la dynamique du système est non linéaire et sensible à des oscillations instables, voire chaotiques. Dans ce rapport, la stabilité des systèmes de remorquage de débris spatiaux est étudiée en considérant les forces aérodynamiques. Les équations de mouvement sont dérivées à l'aide de la méthode Lagrangien dans le référentiel de l'engin spatial où, le mouvement est confiné au plan orbital bidimensionnel et le mouvement de l'engin spatial est prescrit. Une simulation numérique est réalisée pour divers cas afin d'étudier le comportement des points d'équilibre, les oscillations de l'ancrage et les méthodes de stabilisation. Les principaux paramètres d'intérêt sont les propriétés aérodynamiques des débris, l'orientation de l'ancrage et les effets de la grandeur et de la direction de la force appliquée au vaisseau spatial. Ces méthodes explorent l'effet de l'aérodynamique sur les systèmes d'engins satellitaires ancrés, qui demeure peu étudié. De plus, la modélisation du système dans le référentiel de l'engin spatial plutôt que celui du centre de masse du système facilite l'utilisation de ces résultats dans la conception du système de contrôle, car ce point peut être plus facilement suivi. Comprendre le comportement et la dynamique du système est essentiel à la conception de systèmes d'élimination des débris spatiaux, de systèmes de contrôle, de missions et de satellites.

# Acknowledgements

The research accomplished for this thesis would not have been possible without the invaluable guidance of my supervisor, Professor Arun Misra. His feedback and continual support were always appreciated during the duration of this project, and I am grateful to have had the opportunity to work on this research. As well, I thank my friend, Thierry Al Akl, who graciously edited the French translation of my abstract. Finally, I am lucky to have such exceptional family and friends; everyday I am thankful for their support.

# Table of Contents

Abstract . . . . .	i
Abrégé . . . . .	ii
Acknowledgements . . . . .	iii
List of Figures . . . . .	vii
List of Tables . . . . .	viii
<b>1 Introduction</b>	<b>1</b>
1.1 Space Debris . . . . .	1
1.2 Tethered Systems . . . . .	4
1.3 Previous Work . . . . .	6
1.4 Scope and Outline of the Project . . . . .	8
<b>2 System Definition</b>	<b>9</b>
2.1 Overall Schematic and Assumptions . . . . .	9
2.2 Motion of the Space Tug-Debris System . . . . .	11
2.2.1 Velocity . . . . .	12
2.2.2 Energy . . . . .	14
2.2.3 Generalized Forces . . . . .	17
2.2.4 Lagrangian Formulation . . . . .	20
2.3 Implementation . . . . .	21
<b>3 Numerical Simulation Results</b>	<b>25</b>
3.1 Validation . . . . .	26

3.2	Preliminary Results . . . . .	28
3.3	Effect of Thrust . . . . .	33
3.4	Effect of Aerodynamics . . . . .	37
3.4.1	Maximum Aerodynamic Force . . . . .	37
3.4.2	Maximum Overall Force . . . . .	41
3.4.3	Aerodynamics with Increasing Lift . . . . .	43
3.4.4	Shifting Equilibrium . . . . .	45
3.5	Stabilization with Force . . . . .	46
3.6	Discussion . . . . .	49
<b>4</b>	<b>Conclusion</b>	<b>51</b>
<b>A</b>	<b>Additional Plots</b>	<b>57</b>
A.1	Preliminary Results: Conservation of Energy . . . . .	57
A.2	Case 7: Effects of Aerodynamics . . . . .	60
<b>B</b>	<b>MATLAB Code</b>	<b>61</b>

# List of Figures

1.1	Catalogued density of debris in LEO as a function of Altitude between 2008-2020 [16]	2
1.2	Threat of impact of space debris [6]	3
1.3	Tethered space debris removal system [15]	4
1.4	Diagram depicting the components of tether-based ADR	5
1.5	Tether-tug system in the frame of reference of the system's centre of mass [3]	7
2.1	Overall schematic of system	10
2.2	Labeled schematic of relevant variables	11
3.1	Case 9: Local vertical - Validation: Work and change in energy vs time	27
3.2	Case 9: Local vertical - Validation: Histogram	28
3.3	Case 1: Local vertical - important orbital parameters	30
3.4	Case 1: Local horizontal - important orbital parameters	30
3.5	Case 1: Local vertical - behaviour of debris angle	31
3.6	Case 1: Local horizontal - behaviour of debris angle	32
3.7	Case 1: Local vertical - non-dimensional potential energy vs tether angle	33
3.8	Case 2: Local vertical - important orbital parameters	34
3.9	Case 3: Local vertical - important orbital parameters	34
3.10	Case 2: Local horizontal - important orbital parameters	35
3.11	Case 3: Local horizontal - important orbital parameters	35
3.12	Case 3: Local horizontal - non-dimensional potential energy vs tether angle	36

3.13	Case 4: Local vertical - magnitude of applied aerodynamic forces . . . . .	38
3.14	Case 4: Local vertical - behaviour of debris angle . . . . .	39
3.15	Case 4: Local vertical - important orbital parameters . . . . .	40
3.16	Case 4: Local horizontal - important orbital parameters . . . . .	40
3.17	Case 5: Local vertical - important orbital parameters . . . . .	42
3.18	Case 5: Local horizontal - important orbital parameters . . . . .	42
3.19	Case 6: Local vertical - important orbital parameters . . . . .	44
3.20	Case 6: Local horizontal - important orbital parameters . . . . .	44
3.21	Case 8: Local horizontal - important orbital parameters . . . . .	45
3.22	Case 8: Local horizontal - non-dimensional potential energy . . . . .	46
3.23	Case 9: Local vertical - important orbital parameters . . . . .	48
3.24	Case 9: Local horizontal - important orbital parameters . . . . .	48
A.1	Potential Energy vs Time from Local Vertical in Free Oscillation (Case 1) . .	57
A.2	Kinetic Energy vs Time from Local Vertical in Free Oscillation (Case 1) . . .	58
A.3	Potential Energy vs Time from Local Horizontal in Free Oscillation (Case 1)	58
A.4	Kinetic Energy vs Time from Local Horizontal in Free Oscillation (Case 1) .	59
A.5	Case 7: Local vertical - important orbital parameters . . . . .	60
A.6	Case 7: Local horizontal - important orbital parameters . . . . .	60

# List of Tables

1.1	Approximate size and quantity of space debris in orbit as of 2015 [20] . . . .	3
2.1	Constants used to construct the density model [5] . . . . .	19
2.2	Constant physical parameters used throughout test simulations . . . . .	21
2.3	Constant physical parameters used throughout test simulations . . . . .	22
2.4	IVP Initial Conditions . . . . .	23
3.1	Values of Applied Force Parameters for Shown Cases . . . . .	25

# Nomenclature

## Abbreviations

ADR Active debris removal

ESA European Space Agency

IVP Initial value problem

LEO Lower Earth orbit

ODE Ordinary differential equation

## Constants

$\mu$  Standard gravitational parameter  $3.986 \times 10^{14} m^3/s^2$

$R_E$  Radius of the Earth  $6.371 \times 10^6 m$

## Variables

$A$  Cross-sectional area of the debris

$\alpha$  Inclination of the tether relative to local vertical (CCW)

$\beta$  Inclination of the thrust relative to local horizontal (CCW)

$C_D$  Drag coefficient of the debris

$C_L$  Lift coefficient of the debris

$F_T$	Thrust on the space tug
$I_G$	Centroidal second moment of inertia of the debris
$l$	Length of the tether
$m_D$	Mass of the debris
$m_T$	Mass of the space tug
$\phi$	Inclination of the debris relative to local vertical (CCW)
$\rho$	Density of air
$R_D$	Radial distance of the debris
$R_T$	Radial distance of the space tug
$\theta$	True anomaly of the space tug

# Chapter 1

## Introduction

### 1.1 Space Debris

For over sixty years, space-based technologies have enriched society with information from space exploration, satellite networks, and astronomical research. With the growing privatization of the space sector, the world is seeing a large increase in space traffic, particularly with the launching of large satellite networks. Innovation in the space sector is looking to expand the usefulness of Earth's orbits; improving internet access, navigation systems, telecommunications, and meteorologic observation. Furthermore, as government agencies prepare for larger space exploration missions to the moon and further; space research, policy, and safety is of utmost importance.

After decades of space launches, the lower Earth orbit (LEO) has become overrun with dead satellites, abandoned rocket stages, and other discarded remnants from previous space missions all known as space debris [9]. Space debris, also known as space junk or orbital debris, are any man-made non-functional objects orbiting the Earth's surface. The generation of space debris originates primarily from human activities leaving objects such as discarded rocket stages, protective launch vehicle fairings, and abandoned satellites. Furthermore, collisions between debris objects themselves have the potential to result in "Kessler Syndrome," where a series of impacts between large debris create a multitude

of smaller debris [9,10]. As of 2020, over 23,000 debris objects were being tracked, and it is estimated that millions more are unaccounted for [16]. There exists a wide variety of sizes of debris tabulated in table 1.1 with their estimated quantities in orbit as of 2015 [20]. Figure 1.1 illustrates the catalogued density of debris as a function of altitude in LEO [16]. Due to such high object density in orbits common to satellite networks, active spacecraft have an increasing risk of colliding with debris [4,9]. As of now, space stations and active satellites such as the International Space Station (ISS) (which located at an altitude of 408km) are being manually maneuvered to avoid flying debris, contributing to the unnecessary depletion of resources [10].

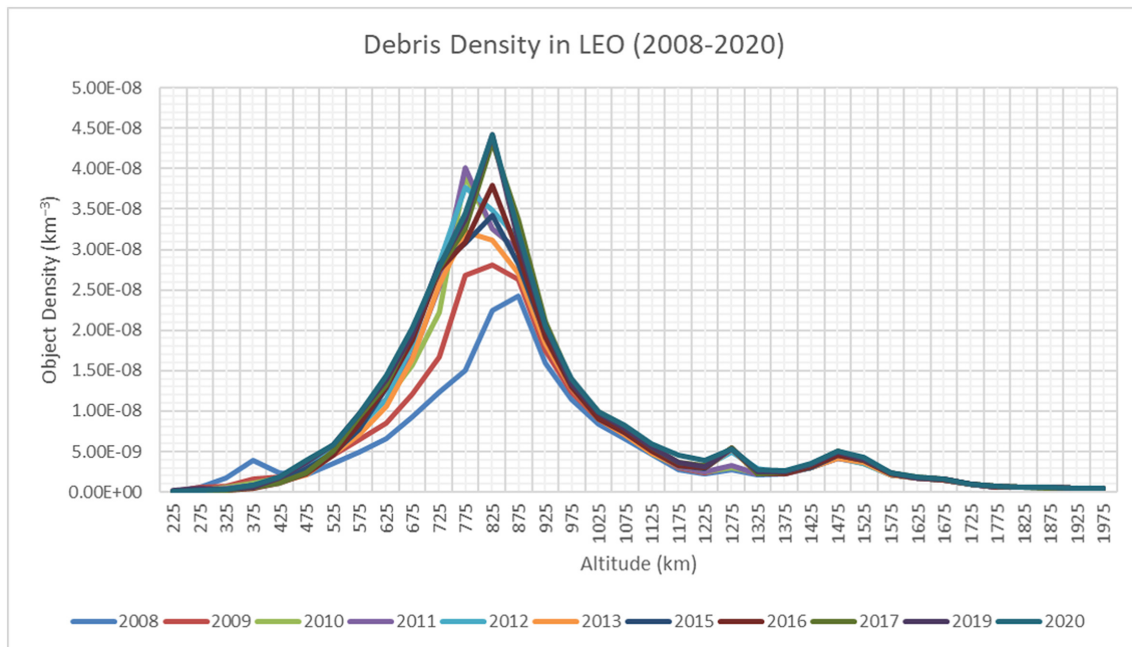


**Figure 1.1:** Catalogued density of debris in LEO as a function of Altitude between 2008-2020 [16]

Space debris poses a significant risk to active spacecraft. For example, a piece of debris weighing as little as 300mg and size 2 cm<sup>3</sup> can reach speeds as high as 15km/s without air resistance, giving it an equivalent kinetic energy twenty-three times that of dynamite [18]. Figure 1.2 shows an example of experiments done by the European Space Agency (ESA) into the potential hazards of hyper-velocity impacts in orbit [6]. One notable collision incident involving space debris is the 2009 collision between the operational Iridium 33

communications satellite and the defunct Cosmos 2251 satellite in low Earth orbit. This collision was the first time two satellites are known to have collided in orbit. The event created over 1,300 tracked pieces of debris [8].

**Table 1.1:** Approximate size and quantity of space debris in orbit as of 2015 [20]

Name	Size (cm)	Approximate Quantity of Debris in Orbit
Large	>10	23,000
Medium	1-10	600,000
Small	0.1-1	70 to 80 million
Microscopic	<0.1	$10^{13} - 10^{14}$

Despite space agencies' previous negligence of this issue, mounting concern regarding dangerous collisions and Kessler Syndrome has spurred awareness and research into methods of debris removal. Active debris removal (ADR) is the disposal of abandoned orbiting objects through external influence either by de-orbiting them, moving them to lower orbit, or destroying them. This often involves directly influencing the dynamics of the object by manipulation or force [10]. Active space debris removal using a tug is one promising technique for removing space debris [13]. Tether-based removal systems are relatively simple; technologically ready for implementation and testing; applicable to a variety of debris shapes and sizes; and cost-effective [10].

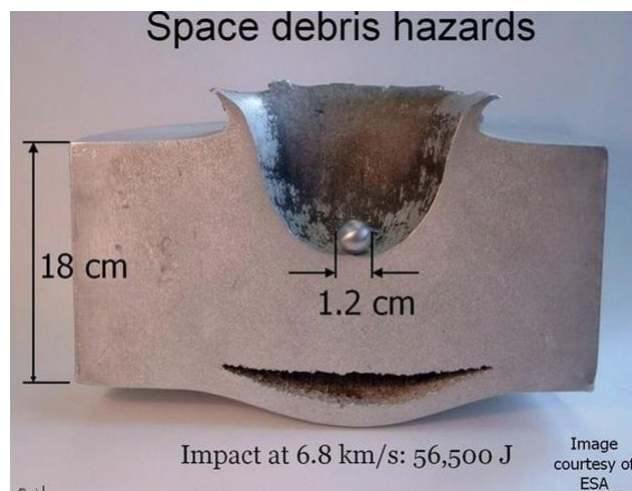


**Figure 1.2:** Threat of impact of space debris [6]

End of life design strategies in space debris refers to the consideration of the disposal of spacecraft and satellites at the end of their operational life. Key elements of this design mentality are designing systems which are conducive to typical debris removal methods or even have a plan for removal built into the design of the craft itself. Such strategies include material and geometry selection, mission design, or even the inclusion of additional forms of propulsion to lower the craft to disposal orbits [10].

## 1.2 Tethered Systems

Space tethers are extremely long thin cables which connect objects in space, they can have lengths from a few hundreds of meters to a few kilometers (see figure 1.3). These tethers are typically made from special materials able to withstand the conditions of space as well as be strong enough to perform particularly strenuous tasks [17]. Conductive tethers are space tethers made of conductive metal fibres or materials which are able to make use of the Earth's magnetic field or radiation belts to generate propulsion [10].



**Figure 1.3:** Tethered space debris removal system [15]

Non-conductive space tethers serve a variety of purposes. Largely, such tethers couple two or more space objects for the exchange of energy or momentum for towing or

propulsion. As well, tethered systems can enable groups of satellites to fly in formations. Formation flying is useful for environmental studies of the cosmos as well as Earth observation [10,14].

Space debris removal using a tether employs a powered spacecraft named a space “tug” which attaches to a target debris using a tether. By applying thrust, the tug then tows the debris to a disposal orbit where it will lose momentum and fall towards the Earth to be burned up in Earth’s atmosphere. Debris capture by this method is often done via tether-net capture or harpoon capture, the dynamics of which are the subject of many studies [13].

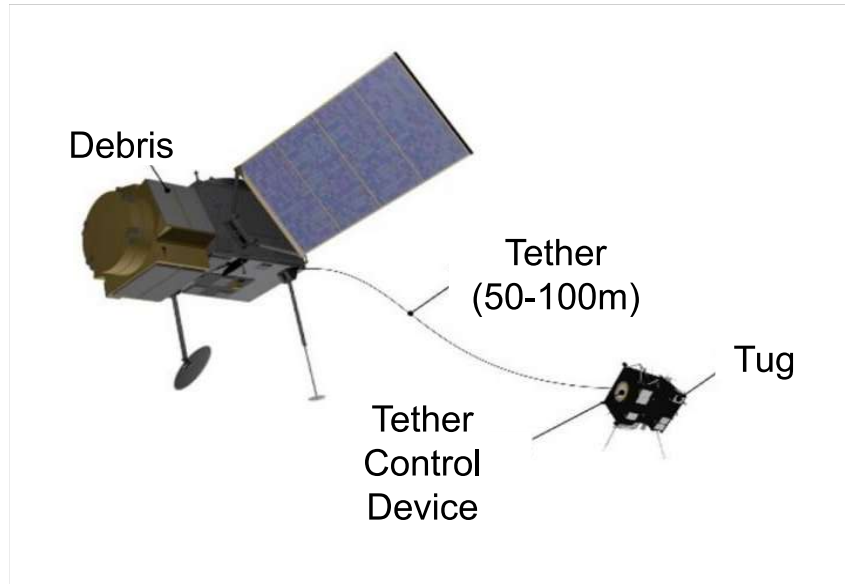


**Figure 1.4:** Diagram depicting the components of tether-based ADR

This method of ADR is controlled and gradual and aims to avoid the generation of new debris. This method is also able to de-orbit larger pieces of debris and, if equipped with multiple tethers or by using a tether-net, can de-orbit multiple debris in one mission. The opportunity to de-orbit multiple debris at once, as well as the low price point of tethers, make tether-based ADR an economically promising option for ADR [10,13].

The dynamics of tethered systems is nonlinear due to the presence of gravitational forces, tether dynamics, atmospheric drag, coupled variables, and the consideration of three gravitational bodies, among others. The non-linearity of tethered systems complicates their use engineering as they are vulnerable to chaotic oscillations. Unstable oscillations are liable to put strain on the system as a whole, causing the tether to snap or complicating control system design as well as mission design. There are many factors to be considered when modelling tethers in space. For example, material properties such as mass, density, and elasticity as well as dynamic properties with respect to tension, bending, and slack in the tether can be difficult to imitate [13]. As a result, tethered systems are difficult to predict analytically. Thus in-depth study is needed to understand the dynamics of the system in response to different parameters as well as initial conditions to assess the feasibility of tethered systems and their stability.

### **1.3 Previous Work**

The inherent usefulness of tethered systems make their study particularly important considering their complex, nonlinear, and chaotic dynamics in response to a variety of different factors. There are many factors that impact the stability of the system: orientation of the tether, the orbital elements of the system, thrust of the tug, properties of the tether, aerodynamic drag, properties of the debris, etc. Numerous studies have already examined many of the variables listed above, making a variety of simplifying assumptions [1–3, 14, 19]. Previous work has identified configurations near local vertical as typically stable systems and those near local horizontal as typically unstable. These observations make these initial conditions of particular interest in future work.

Study of the tug-debris system is often defined in the frame of reference of the centre of mass of the system [2,3,14] as seen in figure 1.5. It was determined early in the research of this method the effects of orbital parameters as well as thrust on the stability of the system and the existence of equilibrium configurations [3]. Equilibrium configurations refer

specifically to the orientation of the tether in the reference frame. Chiefly, considering a local vertical local horizontal (LVLH) orbital plane, tether configurations wherein the tether approaches these axes are of particular interest. As well, the properties of the tether itself such as length [14] and elasticity [7] are of interest as they contribute to longitudinal and transverse tether oscillations.

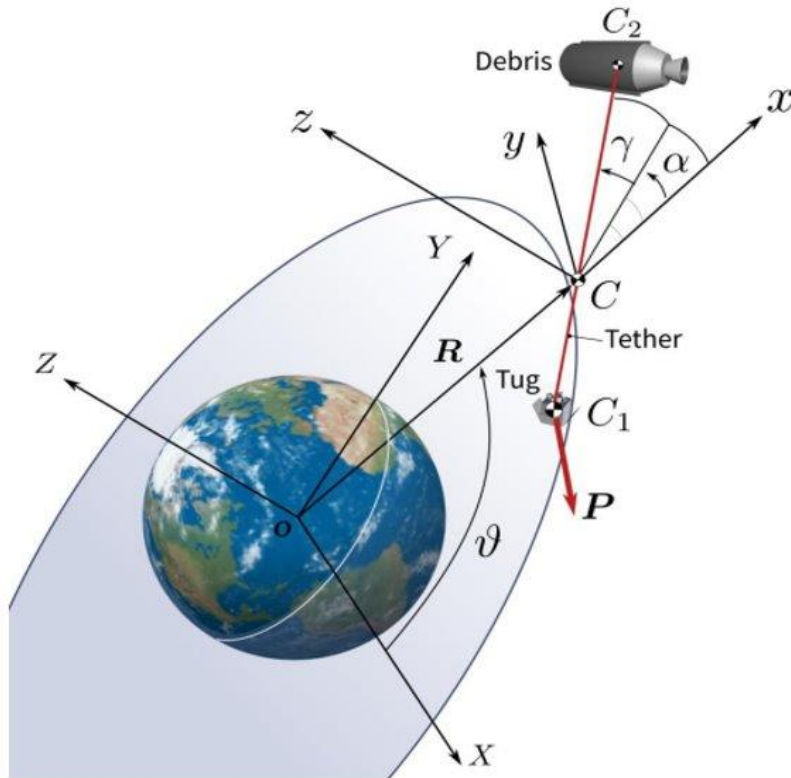


**Figure 1.5:** Tether-tug system in the frame of reference of the system's centre of mass [3]

The effect of aerodynamic drag present in LEO on the tug-debris system is one parameter that has not been studied in detail [2]. Specifically, only the transportation stage (towing from operational orbit to disposal orbit) has been studied in the presence of aerodynamic drag among many other parameters [2]. Aerodynamic forces present in LEO thereby remains an understudied topic in active space debris removal. In addition, modeling the system in the frame of the space tug (rather the centre of mass as done in [2,3,14]) assists in control system design as this location can be more easily tracked.

## 1.4 Scope and Outline of the Project

Dynamic study of the tethered space debris removal system is very important for the success of this method.

This thesis aims to study the stability of space debris towing systems considering aerodynamic drag in LEO. The equations of motion are derived using Lagrangian mechanics where motion is confined to the two-dimensional orbital plane and the space tug has a prescribed orbital motion. By accurately modeling the dynamics of the system, numerical simulation will be conducted for a variety of cases. Parameters of interest include the effects of aerodynamic properties such as surface area, drag coefficient, and lift coefficient on local horizontal and local vertical equilibrium positions. As well, consideration will be given to the use of thrust as a stabilization method.

Posing the question in this fashion, this thesis aims to aid in the design of control systems for space tugs for ADR by placing the frame of reference as the space tug itself. Opting for stable equilibrium positions near local vertical and local horizontal as seen in previous work, the study of the stabilizing effects of thrust magnitude and direction is presented. Furthermore, by considering the physical aerodynamic properties of the debris, spacecraft can be designed with end-of-life strategies which lend themselves to stable tether-based ADR.

# Chapter 2

## System Definition

### 2.1 Overall Schematic and Assumptions

In this section, the Earth-tug-tether system is presented. Using the nomenclature presented in the beginning of the report, the overall system is depicted in figure 2.1. Here, location T marks the location of the space tug, D marks the location of the debris, and E marks the location of the Earth. Accordingly, properties with subscript T refer to those of the space tug and subscript D refers to those of the debris.

The space tug (T) orbits the earth (E) in a counter-clockwise direction attached to debris (D) by a tether. Note the definition of a local vertical—local horizontal (LVLH) coordinate system where the  $\mathbf{k}$  direction is oriented out of the page. The variable  $\theta$  represents the true anomaly of the space tug (T) and is oriented along the positive  $\mathbf{k}$  axis.

Several simplifying assumptions are taken to model the system. Motion is modelled in the frame of reference of the space tug using an LVLH coordinate system. A detailed view of this reference frame is depicted in figure 2.2 where  $\mathbf{i}$  represents the local vertical, oriented along  $\vec{\mathbf{R}}_T$  and perpendicular to this is  $\mathbf{j}$  representing local horizontal. Angles are measured counterclockwise in the positive  $\mathbf{k}$  direction. Tether angle  $\alpha$  and debris angle  $\phi$  are measured from local vertical and the angle of applied force  $\beta$  is measured from local horizontal.

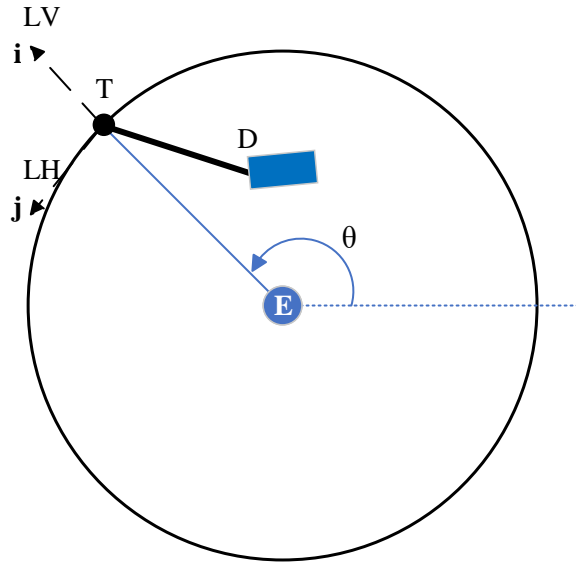


**Figure 2.1:** Overall schematic of system

Assuming the tug as a point mass, analysis is conducted assuming motion is limited to the two-dimensional orbital plane of said tug and that this space tug takes a prescribed circular orbit.

The tether is modelled as a massless rigid body of finite length. This assumption results in the omission of the potential and kinetic energy of the tether. Furthermore, as a rigid body, any elasticity or slack in the tether is neglected.

Lastly, the debris is modelled as a rigid body of arbitrary shape with parametrized properties of mass, moment of inertia about its centre of mass, cross-sectional area, drag coefficient, and lift coefficient. Distance  $d$  represents the distance between the location of tether attachment on the debris D and the centre of mass of the debris G. Considering  $d$  as negligible compared to the length of the tether  $l$  this distance is omitted in several steps of the derivation as seen in following sections.

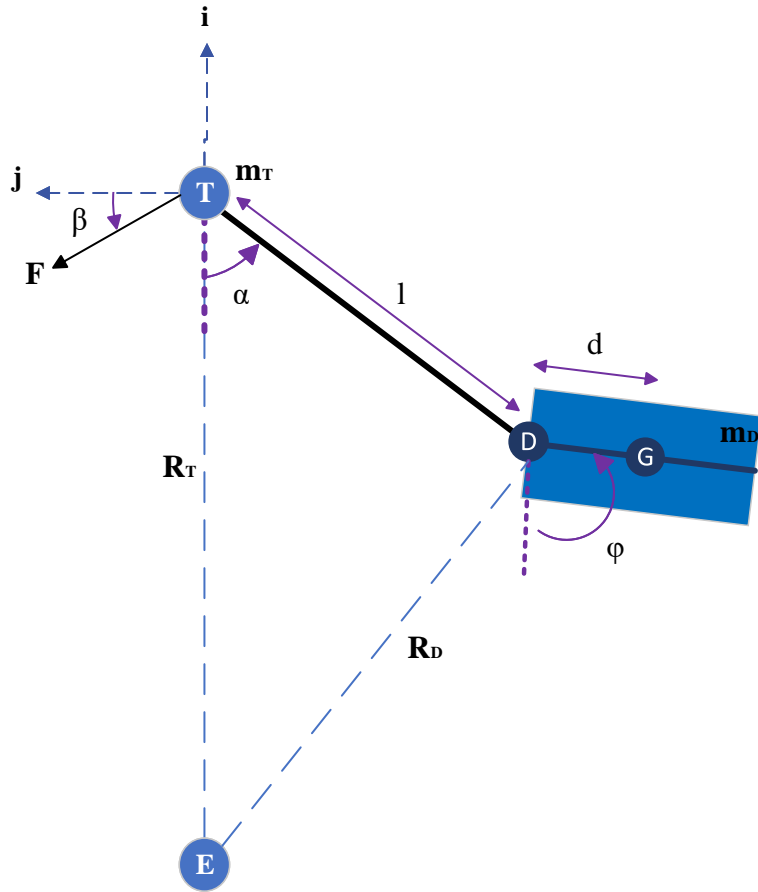


Figure 2.2: Labeled schematic of relevant variables

## 2.2 Motion of the Space Tug-Debris System

In this section, the derivation of the equations of motion governing the system described in the previous section are presented. A Lagrangian approach is employed in four degrees of freedom defined by the generalized coordinates  $R_T$ ,  $\theta$ ,  $\alpha$ , and  $\phi$  depicted visually in figures 2.1 and 2.2. Generalized forces are described in detail below, including thrust force  $\vec{\mathbf{F}}$  shown on figure 2.2 applied at an angle  $\beta$  counterclockwise relative local horizontal. The other forces in consideration are aerodynamic drag and aerodynamic lift described by parameters:  $A$ ,  $C_D$ , and  $C_L$  depicting cross-sectional area, drag coefficient, and lift coefficient of the debris as outlined in the nomenclature section.

Lagrange's equations of motion are derived by the expression

$$\frac{\delta}{\delta t} \left( \frac{\delta T}{\delta \dot{q}_i} \right) - \frac{\delta T}{\delta q_i} + \frac{\delta V}{\delta q_i} = Q_i \quad (2.1)$$

where  $T$  represents the total kinetic energy of the system and  $V$  is the total potential energy of the system. As outlined in the nomenclature, the variables  $q_i$ ,  $\dot{q}_i$  and  $Q_i$  represent the  $i$ th generalized coordinate, generalized velocity, and generalized force, respectively. Evaluating this equation at each of the four generalized coordinates results in a system of four second-order ordinary differential equations (ODEs) representing the governing equations of motion of the system. These equations are then implemented in a numerical simulation in the following sections for analysis.

In the following subsections, the position and velocity terms are presented in terms of the generalized coordinates. Kinetic and potential energy terms are then derived and used to generate the left-hand side of equation 2.1. The expressions for the forces acting on the system are then presented and converted to generalized forces using the previously derived expressions of velocity and position.

### 2.2.1 Velocity

The velocity of the tug is derived based on the movement of the tug along its radial coordinate as well as the tangential velocity which is based on orbital rate and orbital radius of the tug. Considering these effects, the velocity vector of the tug is expressed as

$$\vec{v}_T = \dot{R}_T \vec{i} + \dot{\theta} R_T \vec{j}, \quad (2.2)$$

whose magnitude can be expressed as

$$|v_T| = \sqrt{\dot{R}_T^2 + \dot{\theta}^2 R_T^2}. \quad (2.3)$$

The velocity of the point D on the debris can be derived as a direct result of the velocity of the tug. By adding the relative velocity between the debris and the space tug to the velocity of the space tug, one obtains

$$\vec{v}_D = [\dot{R}_T + l(\dot{\alpha} + \dot{\theta})\sin\alpha]\vec{i} + [\dot{\theta}R_T - l(\dot{\alpha} + \dot{\theta})\cos\alpha]\vec{j}, \quad (2.4)$$

whose magnitude can be expressed as

$$|v_D| = \sqrt{\dot{R}_T^2 + 2\dot{R}_Tl(\dot{\alpha} + \dot{\theta})\sin\alpha + l^2(\dot{\alpha} + \dot{\theta})^2 + \dot{\theta}^2R_T^2 - 2l\dot{\theta}R_T(\dot{\alpha} + \dot{\theta})\cos\alpha}. \quad (2.5)$$

Note that, due to the rotating reference frame, the position of the point D relative point T is expressed as

$$\vec{r}_{D/T} = -l(\cos\alpha\vec{i} + \sin\alpha\vec{j})$$

where the relative rotation is based on the rotation of the tether as well as the orbital rate of the whole system about the Earth resulting in a rotational speed of

$$\omega_{\text{tether}} = (\dot{\alpha} + \dot{\theta})\vec{k}$$

between points T on the tug and D on the debris.

Here, the derivation of the velocity of the centre of mass of the debris (point G) will be derived for completeness. It is assumed that points D and G are sufficiently close such that the relative velocity between these points may be neglected and  $\vec{v}_G \approx \vec{v}_D$ .

Using a similar procedure to the derivation above, the relative velocity  $\vec{v}_{G/D}$  is derived using the relative position and relative rotation between the points G and D. This value is then added to  $\vec{v}_D$  as described in equation 2.4. Again considering the rotation of the debris  $\dot{\phi}$  as well as the orbital rate  $\dot{\theta}$ , it can be shown that

$$\vec{v}_G = [\dot{R}_T + l(\dot{\alpha} + \dot{\theta})\sin\alpha + d(\dot{\phi} + \dot{\theta})\sin\phi]\vec{i} + [\dot{\theta}R_T - l(\dot{\alpha} + \dot{\theta})\cos\alpha - d(\dot{\phi} + \dot{\theta})\cos\phi]\vec{j} \quad (2.6)$$

For the rest of the derivation,  $v_{\vec{G}/D}$  is neglected by assuming  $l$  is large compared to  $d$ . Thus, it is assumed that  $\vec{v}_G \approx \vec{v}_D$ .

## 2.2.2 Energy

### Potential Energy

The gravitational potential energy of both the tug and the debris are presented. Any gravitational energy or elastic energy generated by the tether is neglected by the assumptions presented in section 2.1. The general form of gravitational energy for a point mass is

$$V_T = -\mu \frac{m}{R} \quad (2.7)$$

where  $\mu$  is the standard gravitational parameter of Earth whose value is stated in nomenclature,  $m$  represents the mass of the object being observed, and  $R$  represents the magnitude of the position of said object from the centre of the Earth.

The tug is assumed to be a point mass located by the generalized coordinate  $\tilde{R}_T$  along local vertical. Using the standard gravitational parameter of Earth  $\mu$  whose value is stated in nomenclature, the gravitational potential energy of the tug is

$$V_T = -\mu \frac{m_T}{R_T} \quad (2.8)$$

Similarly, the gravitational potential energy of the debris is derived assuming the mass of the debris is concentrated to the centre of mass of the debris (G). Based on the previous assumption that the centre of mass (G) is sufficiently close to the location of tether attachment (D) the expression for gravitational energy of the debris is simplified to use equation 2.7 by locating it's mass to the point located described by the vector  $\vec{R}_D$  shown in diagram 2.2. The expression

$$V_D = \frac{-\mu m_D}{\sqrt{R_T^2 - 2R_T l \cos\alpha + l^2}} \quad (2.9)$$

is obtained where the orbital radius  $\vec{R}_D$  is described by

$$\vec{R}_D = (R_T - l\cos\alpha)\vec{i} - l\sin\alpha\vec{j}$$

with magnitude

$$R_D = \sqrt{R_T^2 - 2R_Tl\cos\alpha + l^2}.$$

By summing equations 2.8 and 2.9, we obtain the expression for the total potential energy of simplified system as

$$V = -\mu\left(\frac{m_T}{R_T} + \frac{m_D}{\sqrt{R_T^2 - 2R_Tl\cos\alpha + l^2}}\right) \quad (2.10)$$

### Kinetic Energy

The kinetic energy of the tug and the debris are presented. The kinetic energy of the tether is neglected in all respects, by the assumption that it is massless. Energy of the debris is split into translational and rotational. The general form for the translational kinetic energy of a point mass is

$$V_T = \frac{1}{2}mv^2 \quad (2.11)$$

where  $m$  is the mass of the object in motion and  $v$  is the velocity of the point mass. The general form for the rotational energy of a rigid body

$$V_T = \frac{1}{2}I_G\omega^2 \quad (2.12)$$

where  $I_G$  is the moment of inertia of the object in rotation about its centre of mass and  $\omega$  is its angular velocity.

For the derivation of translational kinetic energy of the debris it is again assumed that the centre of mass (G) is sufficiently close to the point of attachment of the tether resulting in the use of the approximation  $\vec{v}_G \approx \vec{v}_D$ . For the rotational energy of the debris, the rotation of the debris about its centre of mass is considered using the moment of inertia

$I_D$  at a distance of  $d$ . The angular velocity of the debris is taken based on the orbital rate of the reference frame  $\dot{\theta}$  as well as the angular velocity of the debris in the LVLH reference frame as shown in figure 2.2 as  $\dot{\phi}$ .

The translational energy of the tug is expressed as

$$T_T = \frac{1}{2}m_T(\dot{R}_T^2 + \dot{\theta}^2 R_T^2) \quad (2.13)$$

where equation 2.3 describes the magnitude of the velocity of the tug.

Similarly, the translational kinetic energy of the debris is expressed as

$$T_{D1} = \frac{1}{2}m_D[\dot{R}_T^2 + 2\dot{R}_T l(\dot{\alpha} + \dot{\theta})\sin\alpha + l^2(\dot{\alpha} + \dot{\theta})^2 + \dot{\theta}^2 R_T^2 - 2l\dot{\theta}R_T(\dot{\alpha} + \dot{\theta})\cos\alpha] \quad (2.14)$$

by using equation 2.5 as the velocity of the point D on the debris and omitting the effects of the relative velocity  $\mathbf{v}_{\tilde{G}/D}$ .

Finally, the rotational kinetic energy of the debris is expressed as

$$T_{D2} = \frac{1}{2}I_G\omega_D^2 = \frac{1}{2}I_G(\dot{\phi} + \dot{\theta})^2 \quad (2.15)$$

by considering rotation of the debris  $\dot{\phi}$  about the debris' centre of mass G as well as the rotation of the reference plane about the earth  $\dot{\theta}$ .

By summing equations 2.13, 2.14 and 2.15 we obtain the the total kinetic energy of the system (T) as

$$\begin{aligned} T &= \frac{1}{2}m_T[\dot{R}_T^2 + \dot{\theta}^2 R_T^2] \\ &+ \frac{1}{2}m_D[\dot{R}_T^2 + 2\dot{R}_T l(\dot{\alpha} + \dot{\theta})\sin\alpha + l^2(\dot{\alpha} + \dot{\theta})^2 + \dot{\theta}^2 R_T^2 - 2l\dot{\theta}R_T(\dot{\alpha} + \dot{\theta})\cos\alpha] \\ &+ \frac{1}{2}I_G(\dot{\phi} + \dot{\theta})^2 \end{aligned} \quad (2.16)$$

### 2.2.3 Generalized Forces

The generalized forces are derived as the right-hand side of the Lagrange equations described by equation 2.1. For each generalized coordinate  $i$  the associated generalized force is described by

$$Q_i = \sum \mathbf{F}_j \cdot \frac{\delta \mathbf{v}_j}{\delta \dot{q}_i} \quad (2.17)$$

for each applied force  $j$ , where  $v_j$  is the velocity at the position of application of force  $F_j$ .

#### Forces

First, the general equations for the applied forces; thrust, aerodynamic drag, and aerodynamic lift, are presented. Thrust is applied to the space tug at point T with a magnitude of  $F$  at an angle  $\beta$  measured counter-clockwise from local horizontal as shown in figure 2.2. In vector form, the applied thrust force is

$$\vec{\mathbf{F}}_{\text{Thrust}} = F(-\sin\beta\vec{\mathbf{i}} + \cos\beta\vec{\mathbf{j}}). \quad (2.18)$$

Aerodynamic drag force acts on the space debris at point G parallel to  $\vec{\mathbf{v}}_D$ . In vector form, aerodynamic drag is described by

$$\vec{\mathbf{F}}_D = -\frac{C_D A \rho}{2} |v_D| \vec{\mathbf{v}}_D \quad (2.19)$$

where  $\vec{\mathbf{v}}_D$  is described by equation 2.4 and  $|v_D|$  is described by equation 2.5. Note the use of the assumption that aerodynamic drag is applied at the location described by  $\vec{\mathbf{R}}_D$  with velocity  $\vec{\mathbf{v}}_D$ , neglecting the influence of distance  $d$ .

Conversely, aerodynamic lift acts on the space debris at point G perpendicular to  $\vec{\mathbf{v}}_D$  and is described by

$$\vec{\mathbf{F}}_L = \frac{C_L A \rho}{2} |v_D|^2 \vec{\mathbf{n}} \quad (2.20)$$

Where  $\vec{n}$  can be described by

$$\vec{n} = \frac{1}{|v_D|} \{ [\dot{\theta}R_T - l(\dot{\alpha} + \dot{\theta})\cos\alpha]\vec{i} - [\dot{R}_T + l(\dot{\alpha} + \dot{\theta})\sin\alpha]\vec{j} \} \quad (2.21)$$

Since aerodynamic drag and aerodynamic lift are applied at the same point, the same generalized velocity will be used in the formulation of equation 2.17. Thus, to simplify analysis and future formulations, equations 2.19 and 2.20 are summed to obtain

$$\begin{aligned} \vec{\mathbf{F}}_{\text{Aero}} = & \left[ \frac{C_L A \rho}{2} |v_D| [\dot{\theta}R_T - l(\dot{\alpha} + \dot{\theta})\cos\alpha] - \frac{C_D A \rho}{2} |v_D| [\dot{R}_T + l(\dot{\alpha} + \dot{\theta})\sin\alpha] \right] \vec{i} \\ & + \left[ -\frac{C_L A \rho}{2} |v_D| [\dot{R}_T + l(\dot{\alpha} + \dot{\theta})\sin\alpha] - \frac{C_D A \rho}{2} |v_D| [\dot{\theta}R_T - l(\dot{\alpha} + \dot{\theta})\cos\alpha] \right] \vec{j} \end{aligned} \quad (2.22)$$

### Lagrange's Generalized Forces

Using force equations 2.18 and 2.22 with velocities  $\vec{v}_T$  and  $\vec{v}_D$  described by equations 2.2 and 2.4 respectively, the generalized forces for each generalized coordinate can be derived. For the first generalized coordinate of  $R_T$ , the generalized force is expressed as

$$Q_{R_T} = -F \sin\beta + \frac{C_L A \rho}{2} |v_D| [\dot{\theta}R_T - l(\dot{\alpha} + \dot{\theta})\cos\alpha] - \frac{C_D A \rho}{2} |v_D| [\dot{R}_T + l(\dot{\alpha} + \dot{\theta})\sin\alpha] \quad (2.23)$$

following equation 2.17.

Similarly, the equation for the generalized force

$$\begin{aligned} Q_\theta = & FR_T \cos\beta \\ & + |v_D| \frac{A\rho}{2} \{ C_L [-l\dot{\theta}R_T \sin\alpha - l\dot{R}_T \cos\alpha - R_T \dot{R}_T - lR_T(\dot{\alpha} + \dot{\theta}) \sin\alpha] \\ & + C_D [l\dot{R}_T \sin\alpha + l^2(\dot{\alpha} + \dot{\theta}) - l\dot{\theta}R_T \cos\alpha - \dot{\theta}R_T^2 + R_T l(\dot{\alpha} + \dot{\theta}) \cos\alpha] \} \end{aligned} \quad (2.24)$$

is obtained for the generalized coordinate  $\theta$ . Then, for the generalized coordinate  $\alpha$ , the expression for generalized force is

$$Q_\alpha = |v_D| \frac{lA\rho}{2} \{C_L \dot{\theta} R_T \sin \alpha + C_D \dot{R}_T \sin \alpha - C_L \dot{R}_T \cos \alpha - C_D \dot{\theta} R_T \cos \alpha + C_D l(\dot{\alpha} + \dot{\theta})\} \quad (2.25)$$

Finally, the equation for the generalized force for the generalized coordinate  $\phi$  is

$$Q_\phi = |v_D| \frac{dA\rho}{2} \{C_L \dot{\theta} R_T \sin \phi + C_L l(\dot{\alpha} + \dot{\theta}) \sin(\alpha - \phi) - C_D \dot{R}_T \sin \phi - C_D l(\dot{\alpha} + \dot{\theta}) \cos(\alpha + \phi) + C_L \dot{R}_T \cos \phi + C_D \dot{\theta} R_T \cos \phi\} \quad (2.26)$$

### Density Model

An exponential model for density  $\rho$  described by

$$\rho = \rho_0 \exp\left(-\frac{R - R_0}{H_0}\right) \quad (2.27)$$

is used in the calculation of air density in atmosphere at orbital radius  $R$ . The model is adapted from work done by Keshmiri, Misra and Modi [12]. The reference value for  $\rho_0$  as well as scale height  $H_0$  are taken from experimental data collected by the European Space Agency at the reference orbital radius  $R_0$  [5]. The relevant constants in this formulation are tabulated in table 2.1.

**Table 2.1:** Constants used to construct the density model [5]

Parameter	Symbol	Value	Units
Reference orbital radius	$R_0$	6771	km
Reference density	$\rho_0$	$2.62 \times 10^{-12}$	kg/m <sup>3</sup>
Scale height	$H_0$	58.2	km

## 2.2.4 Lagrangian Formulation

Following equation 2.1, the left-hand sides of the four governing differential equations of motion are constructed using the total potential energy  $V$  described by equation 2.10 and the total kinetic energy  $T$  described by equation 2.16. Similar to the derivation of generalized forces presented in the previous subsection, the process of deriving equation 2.1 is repeated for each generalized coordinate  $q_i$  equal to  $R_T$ ,  $\theta$ ,  $\alpha$ , and  $\phi$ .

For the generalized coordinate  $R_T$ , the Lagrangian equation of motion is expressed as

$$m_T \ddot{R}_T + m_D [\ddot{R}_T + l(\ddot{\alpha} + \ddot{\theta}) \sin \alpha + \dot{\alpha} l(\dot{\alpha} + \dot{\theta}) \cos \alpha] - m_T \dot{\theta}^2 R_T - m_D (\dot{\theta}^2 R_T - l \dot{\theta}(\dot{\alpha} + \dot{\theta}) \cos \alpha) + \mu \left( \frac{m_T}{R_T^2} + \frac{m_D (R_T - l \cos \alpha)}{(R_T^2 - 2R_T l \cos \alpha + l^2)^{\frac{3}{2}}} \right) = Q_{R_T} \quad (2.28)$$

For the generalized coordinate  $\theta$ , the Lagrangian equation of motion is expressed as

$$m_T \ddot{\theta} R_T^2 + 2m_T \dot{\theta} R_T \dot{R}_T + m_D [\ddot{R}_T l \sin \alpha + \dot{R}_T \dot{\alpha} \cos \alpha + l^2(\ddot{\alpha} + \ddot{\theta}) + \ddot{\theta} R_T^2 + 2\dot{\theta} R_T \dot{R}_T - l \dot{R}_T \dot{\theta} \cos \alpha - l R_T \ddot{\theta} \cos \alpha + l \dot{\alpha} R_T \dot{\theta} \sin \alpha] + I_G (\ddot{\phi} + \ddot{\theta}) = Q_\theta \quad (2.29)$$

For the generalized coordinate  $\alpha$ , the Lagrangian equation of motion is expressed as

$$m_D [\ddot{R}_T l \sin \alpha + \dot{\alpha} \dot{R}_T l \cos \alpha + l^2(\ddot{\alpha} + \ddot{\theta}) - l \ddot{\theta} R_T \cos \alpha - l \dot{\theta} \dot{R}_T \cos \alpha + l \dot{\alpha} \dot{\theta} R_T \sin \alpha - \dot{R}_T l(\dot{\alpha} + \dot{\theta}) \cos \alpha - l \dot{\theta} R_T(\dot{\alpha} + \dot{\theta}) \sin \alpha + \frac{\mu R_T l \sin \alpha}{(R_T^2 - 2R_T l \cos \alpha + l^2)^{\frac{3}{2}}}] = Q_\alpha \quad (2.30)$$

For the generalized coordinate  $\phi$ , the Lagrangian equation of motion is expressed as

$$I_G (\ddot{\phi} + \ddot{\theta}) = Q_\phi \quad (2.31)$$

Equations 2.28, 2.29, 2.30, and 2.31 form the governing equations of motion based on the defined system. With Generalized forces described by equations 2.23, 2.24, 2.25, and 2.26.

## 2.3 Implementation

A numerical solution to the defined system was implemented in MATLAB for simulation and analysis. To fulfill this objective, the following section outlines some of the implementation details regarding the program used where algorithm 1 outlines the entire program architecture.

The equations of motion described by equations 2.28-2.31 and generalized forces 2.23-2.26 construct a system of nonlinear second order ODEs. Using the symbolic toolbox in MATLAB, the generalized coordinates are expressed as symbolic functions of time

$$R_T = R(t), \quad \theta = M(t), \quad \alpha = A(t), \quad \text{and} \quad \phi = p(t).$$

Using this change of variable, the system is translated into MATLAB and the *diff()* function is used to represent the time derivatives of the generalized coordinates [11]. Where

$$\dot{R}_T = \text{diff}(R) \quad \text{and} \quad \ddot{R}_T = \text{diff}(R, 2)$$

and similarly for the other derivatives of the generalized coordinates.

The physical parameters of the system, as shown in figure 2.2 are defined as constants in the program with the values outlined in table 2.2.

**Table 2.2:** Constant physical parameters used throughout test simulations

Parameter	Symbol	Value	Units
Tether length	$l$	50	m
Distance to debris centre of mass	$d$	1	m
Mass of the tug	$m_T$	500	kg
Mass of the debris	$m_D$	200	kg
Moment of inertia of the debris	$I_G$	400	kg · m <sup>2</sup>

The variable parameters being studied are those varying the impact of the generalized forces; thrust, aerodynamic drag, and aerodynamic lift. Table 2.3 tabulates the values of the variables being studied.

**Table 2.3:** Constant physical parameters used throughout test simulations

Parameter	Symbol	Values	Units
Magnitude of thrust	$F$	0, 0.1, 1, 2	N
Angle of applied thrust	$\beta$	0, 10	$^\circ$
Cross-sectional area	$A$	0, 1, 5	$\text{m}^2$
Drag coefficient	$C_D$	0, 2	-
Lift coefficient	$C_L$	0, 0.2, 0.5	-

Following the definition of the governing equations in MATLAB, the function *odeToVectorField* is used to convert the system to state space form [11]. State space form of this system is characterized by a system of eight first-order ODEs. Furthermore, in equations with coupled variables, desired variables are isolated such that each function is composed of only first-derivative terms. This system of symbolic equations is stored in the variable *system* (right) with the order of original variable names stored as an array 'Y' in the variable named *variables* (left) defined as

$$\begin{array}{ll}
 Y_1 = R & \frac{\delta Y_1}{\delta t} = Y_2 \\
 Y_2 = \frac{\delta R}{\delta t} & \frac{\delta Y_2}{\delta t} = f(Y) \\
 Y_3 = M & \frac{\delta Y_3}{\delta t} = Y_4 \\
 Y_4 = \frac{\delta M}{\delta t} & \frac{\delta Y_4}{\delta t} = f(Y) \\
 Y_5 = A & \frac{\delta Y_5}{\delta t} = Y_4 \\
 Y_6 = \frac{\delta A}{\delta t} & \frac{\delta Y_6}{\delta t} = f(Y) \\
 Y_7 = p & \frac{\delta Y_7}{\delta t} = Y_4 \\
 Y_8 = \frac{\delta p}{\delta t} & \frac{\delta Y_8}{\delta t} = f(Y)
 \end{array}$$

Using the MATLAB function *matlabFunction()*, the system of symbolic state space equations is converted to a callable MATLAB function by the handle name *State space* [11].

Finally, the function *ode45* is used to numerically solve the system given as an initial value problem (IVP) by supplying a desired time-frame and a set of initial conditions. Table 2.4 outlines the initial conditions used for each iteration. Note that all initial conditions are the same between iterations apart from initial tether angle  $\alpha$  which varies be-

tween initial conditions of near local vertical (0.1 radians) and near local horizontal (1.67 radians).

The initial orbital rate  $\dot{\theta}$  is determined by a simplified version of Kepler's Third Law

$$\dot{\theta} = \sqrt{\frac{\mu}{R_T^3}} \quad (2.32)$$

for the orbital rate of an object in a circular orbit of radius  $R_T$  where  $R_T$  is the initial orbital radius of the tug as listed in table 2.4.

**Table 2.4:** IVP Initial Conditions

Parameter	Symbol	Values	Units
Orbital radius	$R_T$	6771	km
True anomaly	$\theta$	0	rad
Tether angle	$\alpha$	0.1 or 1.67	rad
Debris angle	$\phi$	0	rad
Radial Velocity	$\dot{R}_T$	0	km/s
Orbital Rate	$\dot{\theta}$	0.00113	rad/s
Tether angular velocity	$\dot{\alpha}$	0	rad/s
Debris angular velocity	$\dot{\phi}$	0	rad/s

The function *ode45* employs typically a Runge-Kutta method, an iterative integration scheme, to solve a given IVP. The fourth-order Runge-Kutta method (RK4) is one of the most widely used due to its high accuracy and low computational cost. The MATLAB function *ode45* uses RK4 with adaptive time stepping which dynamically adjusts step size to maximize both efficiency and accuracy [11].

The function *ode45* then returns the solution *sol* which contains the time stamps  $t$  as well as the integrated results for each generalized coordinate  $R_T$ ,  $\theta$ ,  $\alpha$ , and  $\phi$  as well as generalized velocities  $\dot{R}_T$ ,  $\dot{\theta}$ ,  $\dot{\alpha}$ , and  $\dot{\phi}$ . This data is then plotted for analysis in the following section.

---

**Algorithm 1** Dynamical System Architecture

---

1: Symbolic functions:  $R(t), M(t), A(t), p(t)$

2: **Lagrange's Equations**

3:  $Equation1 \leftarrow \frac{\delta}{\delta t} \left( \frac{\delta T}{\delta \dot{R}_T} \right) - \frac{\delta T}{\delta R_T} + \frac{\delta V}{\delta R_T} = Q_{R_T}$

4:  $Equation2 \leftarrow \frac{\delta}{\delta t} \left( \frac{\delta T}{\delta \dot{\theta}} \right) - \frac{\delta T}{\delta \theta} + \frac{\delta V}{\delta \theta} = Q_{\theta}$

5:  $Equation3 \leftarrow \frac{\delta}{\delta t} \left( \frac{\delta T}{\delta \dot{\alpha}} \right) - \frac{\delta T}{\delta \alpha} + \frac{\delta V}{\delta \alpha} = Q_{\alpha}$

6:  $Equation4 \leftarrow \frac{\delta}{\delta t} \left( \frac{\delta T}{\delta \dot{\phi}} \right) - \frac{\delta T}{\delta \phi} + \frac{\delta V}{\delta \phi} = Q_{\phi}$

7:  $[system, variables] \leftarrow \text{odeToVectorField}(Equation1, Equation2, Equation3, Equation4)$

8:  $State\ space \leftarrow \text{matlabFunction}(system, 'vars', \{ 't', 'Y' \})$

9:  $sol \leftarrow \text{ode45}(M, timespan, system_0s)$

---

All documentation relating to the functions used in the formulation of these simulations can be found on the main MATLAB website [11].

# Chapter 3

## Numerical Simulation Results

In this chapter, results are presented for the numerical simulation of nine test cases near both local horizontal and local vertical. Parameters for each test case are outlined in table 3.1.

Once developing the simulation program, a sweep of all relevant design parameters in the design space (table 2.3) was conducted. All plots were examined to gain an understanding of the trends in behaviour resulting from the application of thrust and aerodynamic force on the defined system. Here, a few interesting cases are highlighted and general conclusions are discussed.

**Table 3.1:** Values of Applied Force Parameters for Shown Cases

	<b>Thrust</b> $F$ (N)	<b>Angle of Applied Thrust</b> $\beta$ ( $^{\circ}$ )	<b>Drag Coefficient</b> $C_D$	<b>Lift Coefficient</b> $C_L$	<b>Cross-Sectional Area</b> $A$ ( $\text{m}^2$ )
<b>Case 1</b>	0	0	0	0	0
<b>Case 2</b>	0.1	0	0	0	0
<b>Case 3</b>	2	0	0	0	0
<b>Case 4</b>	0	0	2	0.5	5
<b>Case 5</b>	2	0	2	0.5	5
<b>Case 6</b>	1	0	2	0	5
<b>Case 7</b>	1	0	2	0.5	5
<b>Case 8</b>	1	10	2	0.5	1
<b>Case 9</b>	2	0	2	0	1

First, a brief validation section is presented using case 9 as an example to show that the numerical model satisfies conservation of energy and the work-energy principle. The preliminary results are then presented in section 3.2 to illustrate that the program simulates expected behaviour in free oscillation based on conservation of energy, work-energy theorem, and knowledge of previous work [1–3, 14]. Preliminary results present the behaviour of the four generalized coordinates in case 1; free oscillation, without any applied forces from either thrust or aerodynamics. Following the validation and identification of the baseline result, the effects of thrust is examined by presenting cases 2 and 3. Subsequently, the effects aerodynamics are examined, presenting case 4 as the maximum effect of aerodynamic forces within the given design space, omitting thrust force. Case 5 presents the extreme case of the design space with maximum force parameters. Cases 6 and 7 then show the varying effects of adding and removing aerodynamic lift. Case 8 demonstrates interesting behaviour over a longer time-span wherein multiple equilibria can be identified for the same initial conditions where the solution to the simulation switches between these equilibrium points. Finally, case 9 displays how the system may be stabilized with force over time for both local horizontal and local vertical configurations. The mechanism behind this stabilization, as well as its drawbacks and potential for implementation will also be discussed in this section.

### 3.1 Validation

In this section, the validation of the numerical model is discussed using case 9 as an example. To begin, any dynamical system must obey conservation of energy and thereby work-energy principle,

$$Work = \Delta E \tag{3.1}$$

where *Work* is work done on the system and  $\Delta E$  is the change in energy of the system. Work can be calculated by multiplying the forces acting on the system by the displacement of the location of applied force in the direction of applied force. In vector form, this

result can be obtained by dot product. In this model, velocities were used to calculate displacement by multiplying by the time-step used in numerical integration. Combining these influences, work was calculated as

$$Work = \vec{F}_{aero} \cdot \vec{v}_D + \vec{F} \cdot \vec{v}_T \quad (3.2)$$

where  $\vec{F}_{aero}$  is represented by equation 2.22,  $\vec{v}_D$  is represented by equation 2.4,  $\vec{F}$  is represented by equation 2.18, and  $\vec{v}_T$  is represented by equation 2.2. Change in energy is simply calculated by summing equations 2.10 and 2.16 and taking the difference at each time-step. On this basis, the numerical program used in this thesis automatically generates the energy plots as well as work-energy plots.

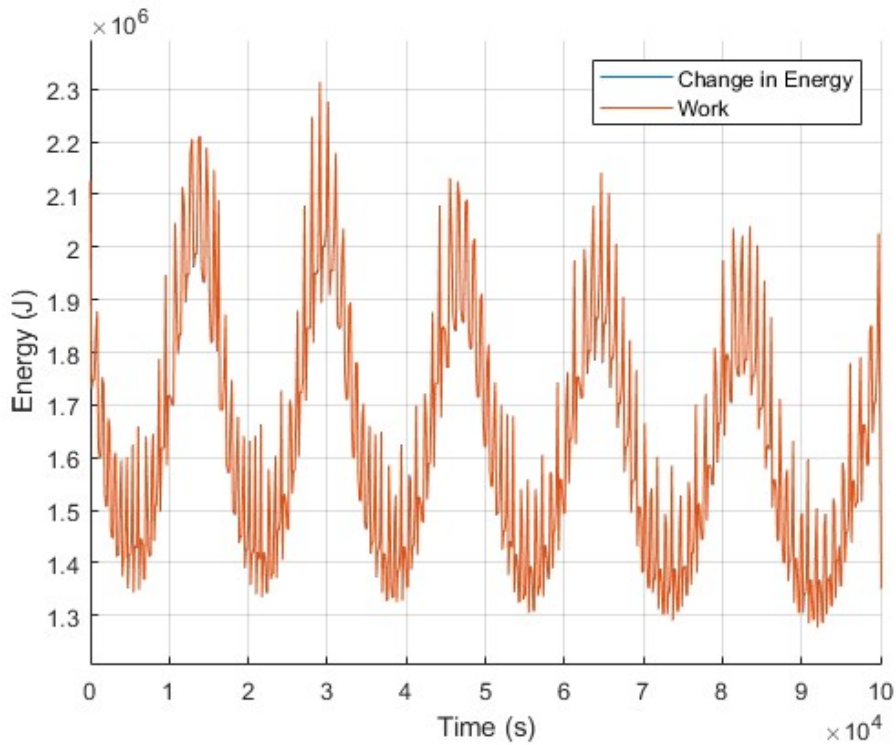


**Figure 3.1:** Case 9: Local vertical - Validation: Work and change in energy vs time

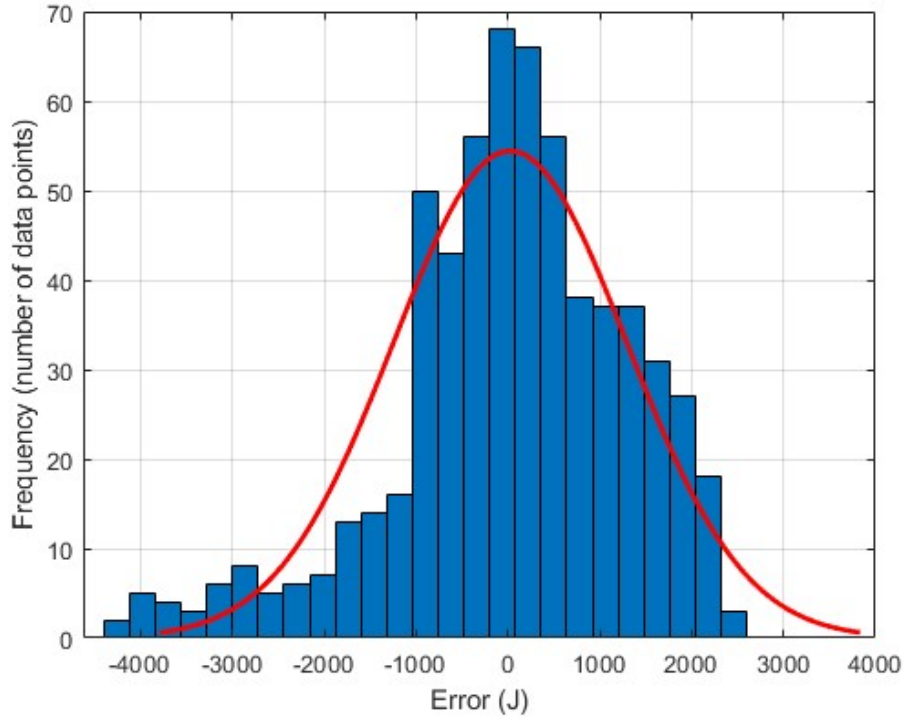


**Figure 3.2:** Case 9: Local vertical - Validation: Histogram

For case 9, figure 3.1 shows the work and change in energy plotted on the same axis over the same time-frame. For this same time-frame, figure 3.2 shows the histogram of tabulated errors in equation 3.1. For this analysis, a standard deviation of 1270.2 J was calculated; 0.0791% the average energy of  $1.6054 \times 10^6$  J. As well, the mean of the error was calculated 24.59 J. With these results consistent across all test cases (within reason) simulation was conducted using the presented numerical model for the described test cases.

## 3.2 Preliminary Results

In this section, the full analysis of Case 1 is presented for local vertical and local horizontal configurations. Figures 3.3 and 3.4 show true anomaly  $\theta$ , orbital rate  $\dot{\theta}$ , tether angle  $\alpha$ , and fluctuations in orbital radius  $R_T$ , which are relevant parameters of interest when studying the orbital system.

In these preliminary cases we verified the expected behaviour of a circular orbit. In both figures 3.3 and 3.4 true anomaly shows a relatively linear trend, with a relatively constant derivative  $\dot{\theta}$ . Oscillations in orbital rate as well as orbital radius are introduced as a result of the effects of the tethered system. By verifying conservation of energy, as seen in appendix A.1, it is expected that energy is transferred between the tug and the debris via the tether. This coupling results in the oscillation seen in orbital rate and orbital radius, but remains bounded due to conservation of energy and the omission of external forces or losses in the system.

Importantly, case 1 sets a baseline for subsequent analysis. As shown in previous work, configurations near local vertical are typically stable and configurations near local horizontal are typically unstable [3]. This result is verified in figures 3.3 and 3.4 by examining the trends in tether angle. In figure 3.3, tether angle is seen to oscillate uniformly about an equilibrium point of  $\alpha = 0$  radians between the given initial angle 0.1 radians and its negative, -0.1 radians. Conversely, figure 3.4 shows unstable behaviour wherein tether angle is seen to decrease over the given time-span. Physically, this implies that the tether does full rotations in the clockwise direction about the space tug from its initial angle of about 1.67 radians.

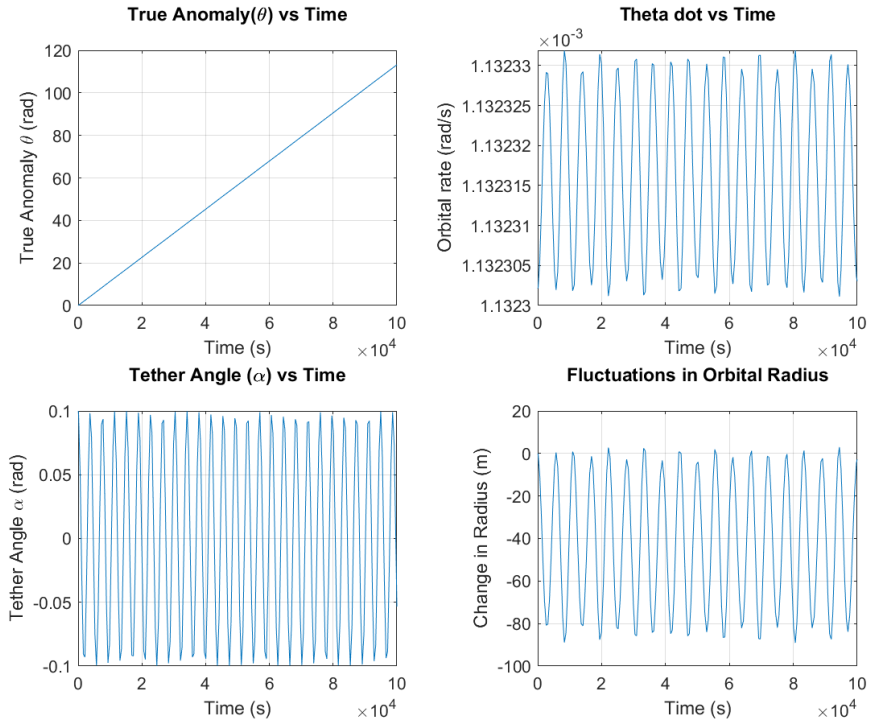


Figure 3.3: Case 1: Local vertical - important orbital parameters

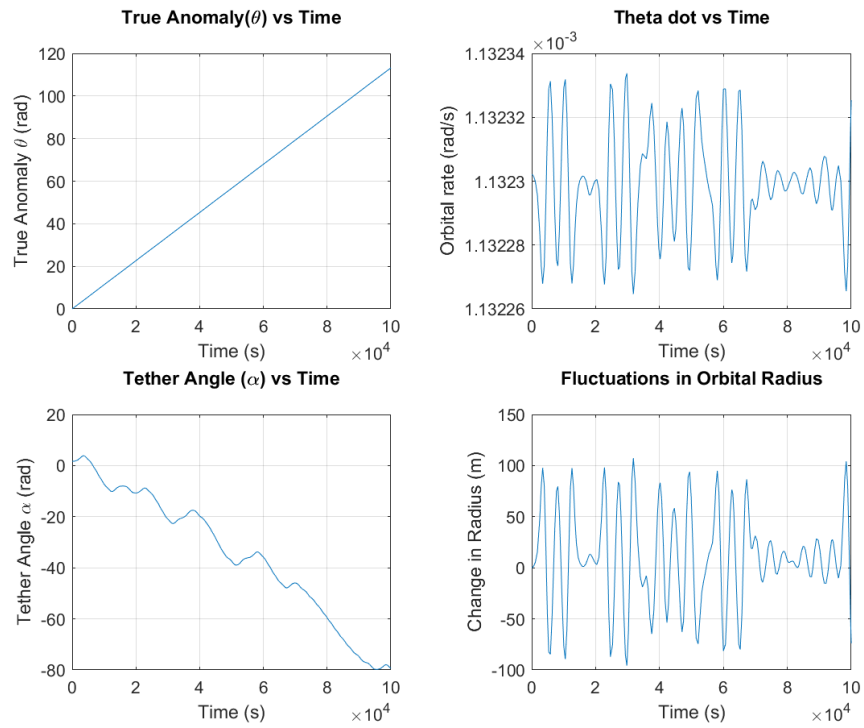
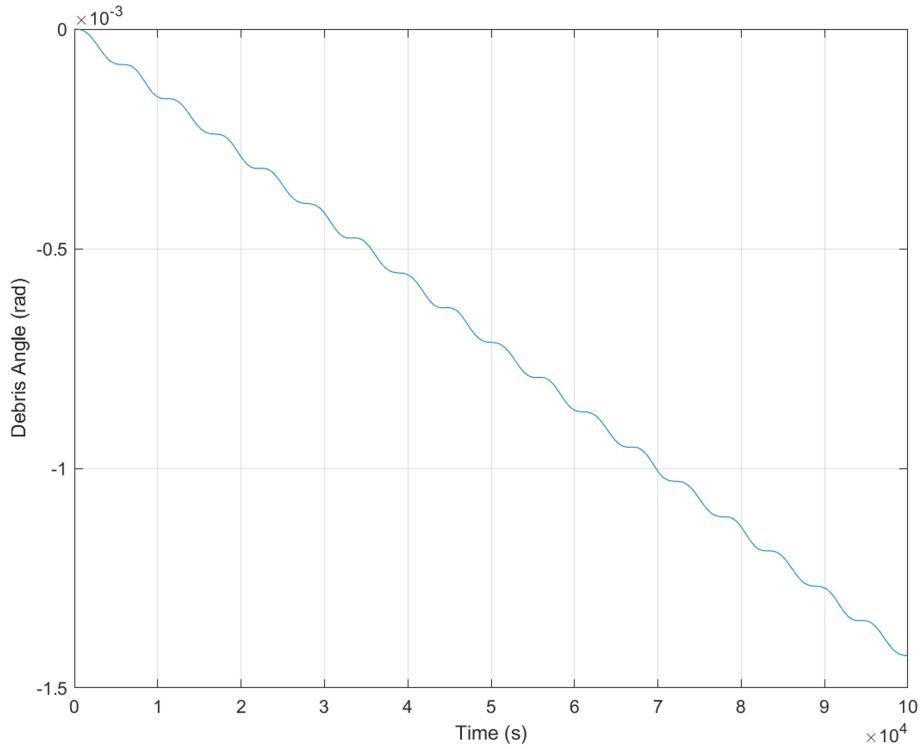


Figure 3.4: Case 1: Local horizontal - important orbital parameters

Figures 3.5 and 3.6 show the behaviour of debris angle  $\phi$  for the baseline case 1. In both cases, from an initial value of  $\phi = 0$  radians, debris angle stays relatively constant, fluctuating between values in the order of magnitude of  $10^{-4}$  radians (in local horizontal) and  $10^{-3}$  radians (in local vertical), both of which are considered negligible. In the case near local vertical, the debris is seen to rotate clockwise as shown in figure 3.5. In the case near local horizontal, the debris is seen to rotate counterclockwise with periods of oscillation as shown in figure 3.6.



**Figure 3.5:** Case 1: Local vertical - behaviour of debris angle

Equilibrium points are identified qualitatively in the following sections by plotting the non-dimensional potential energy  $W$  as

$$W = \frac{F}{m_T l \dot{\theta}^2} \sin \alpha - \frac{3}{2} \cos^2 \alpha \quad (3.3)$$

derived by authors of previous work [3]. By plotting equation 3.3 for the parameters of the studied system against the simulated values of tether angle  $\alpha$  one can identify equilib-

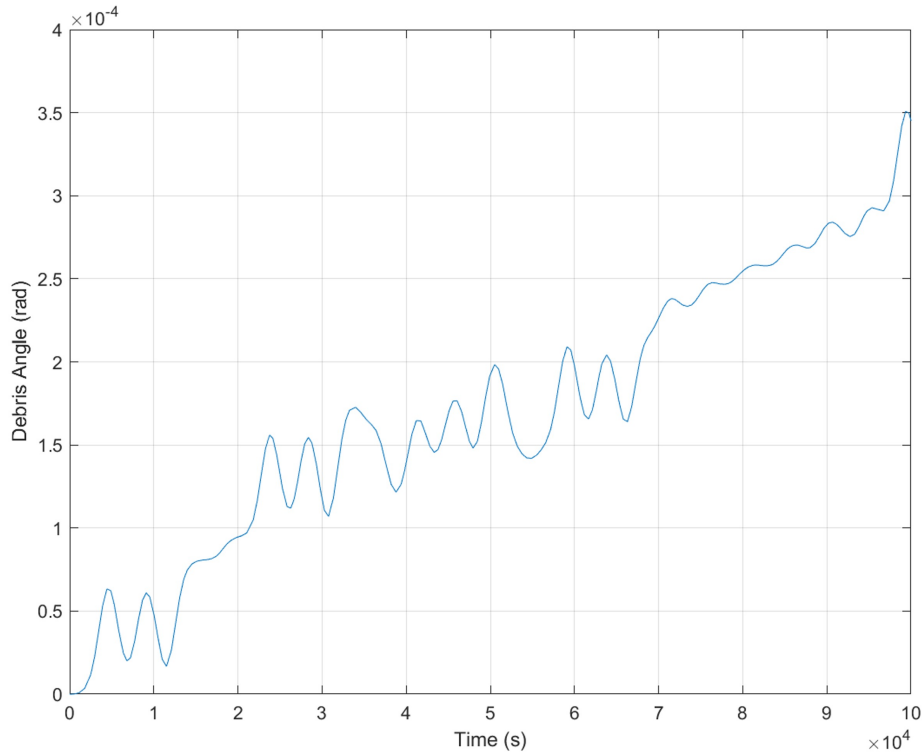


**Figure 3.6:** Case 1: Local horizontal - behaviour of debris angle

rium points by locating the extrema in the plot. Based on theory in nonlinear dynamics, stable equilibria are marked by local minima and unstable equilibria are marked by local maxima.

For case 1 in the stable configuration near local vertical, it can be observed that tether angle in figure 3.3 oscillates about the equilibrium point of 0 radians; exactly local vertical. The same conclusion can be derived by examining the plot of non-dimensional potential energy  $W$  against values of tether angle  $\alpha$  shown in figure 3.7. In this figure, non-dimensional potential energy reaches a local minimum located at a tether angle of 0 radians.

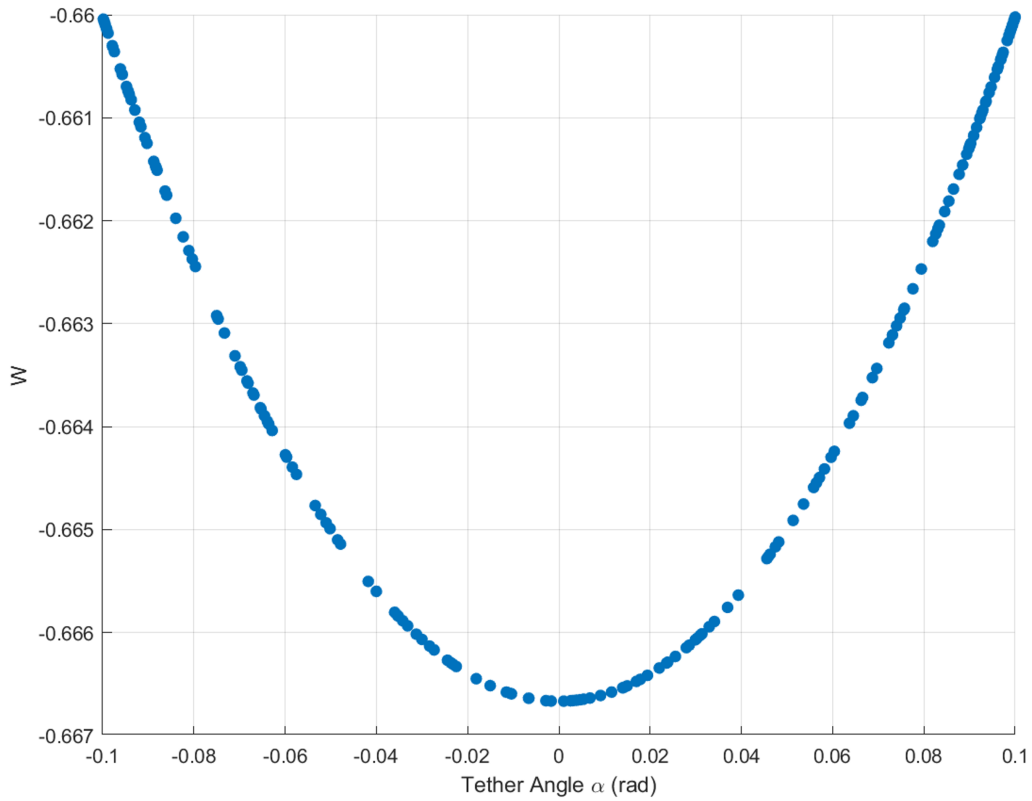


**Figure 3.7:** Case 1: Local vertical - non-dimensional potential energy vs tether angle

### 3.3 Effect of Thrust

In this section, the effect of thrust on the stability of the system is explored by examining cases 2 and 3 as compared to the baseline results presented in section 3.2. Figures 3.8 and 3.9 show cases 2 and 3 from a near-local-vertical initial configuration and figures 3.10 and 3.11 show these cases from a near-local-horizontal initial configuration.

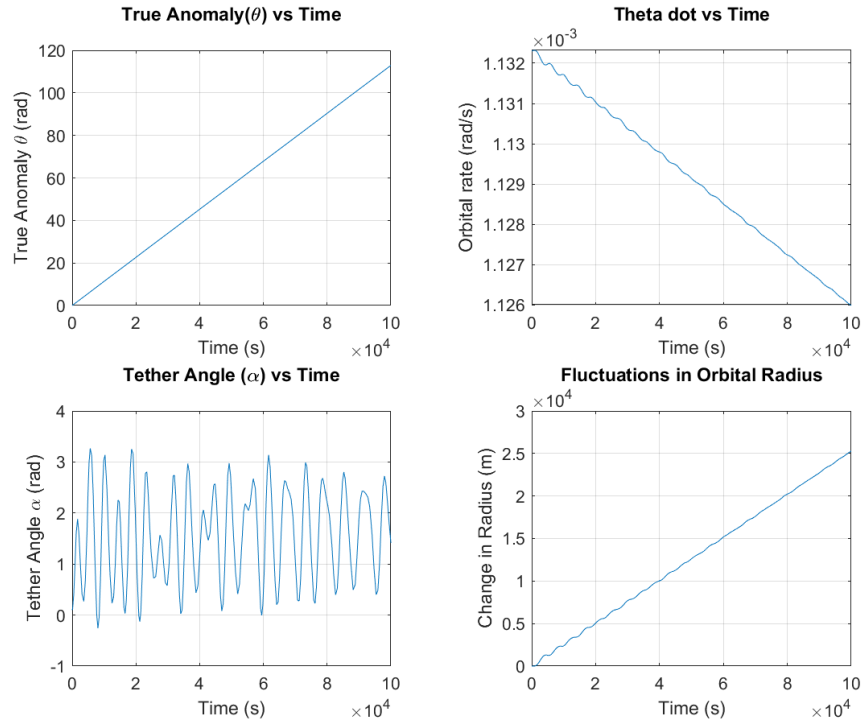


Figure 3.8: Case 2: Local vertical - important orbital parameters

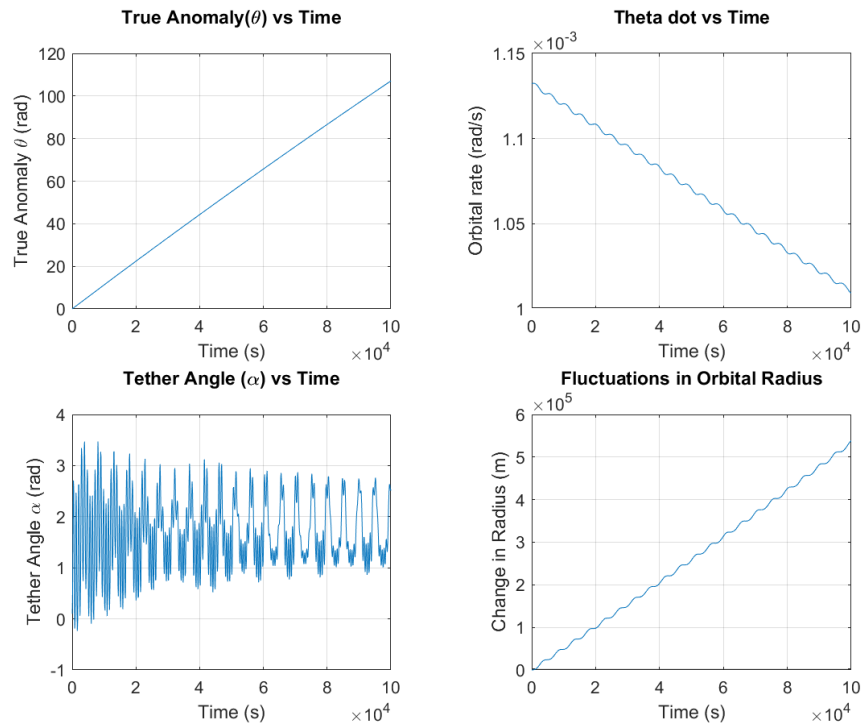


Figure 3.9: Case 3: Local vertical - important orbital parameters

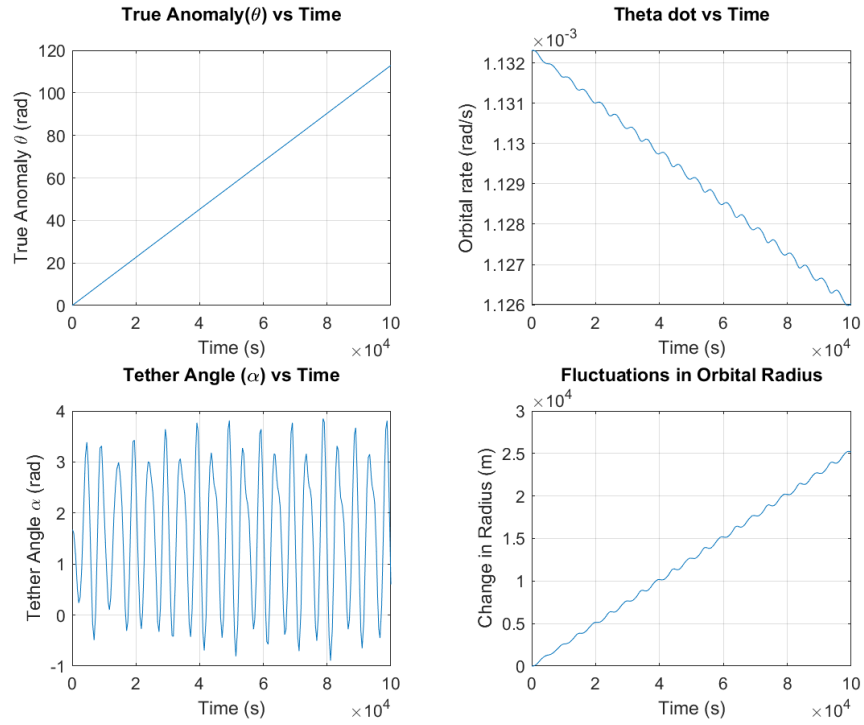


Figure 3.10: Case 2: Local horizontal - important orbital parameters

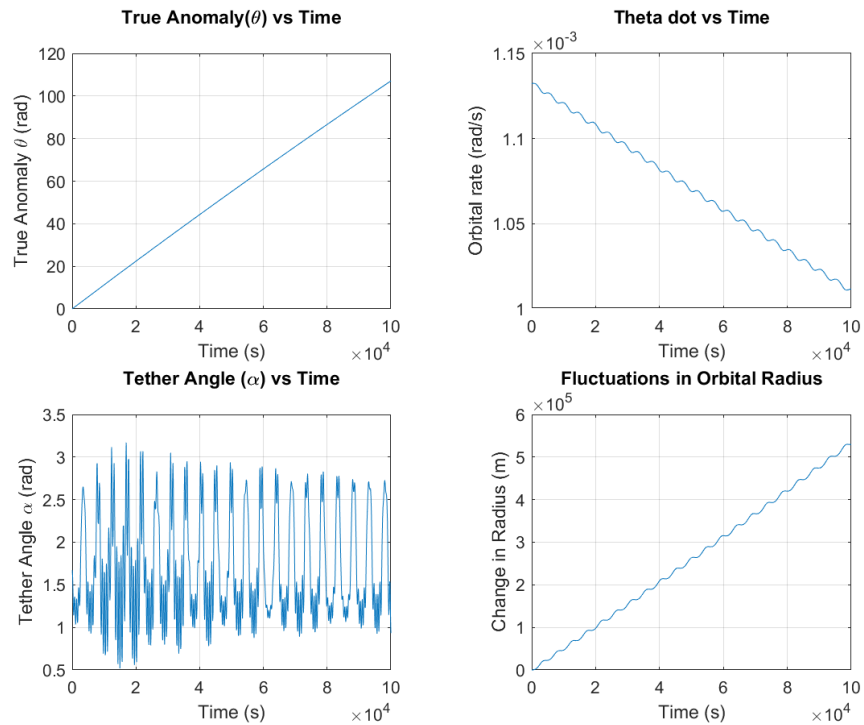
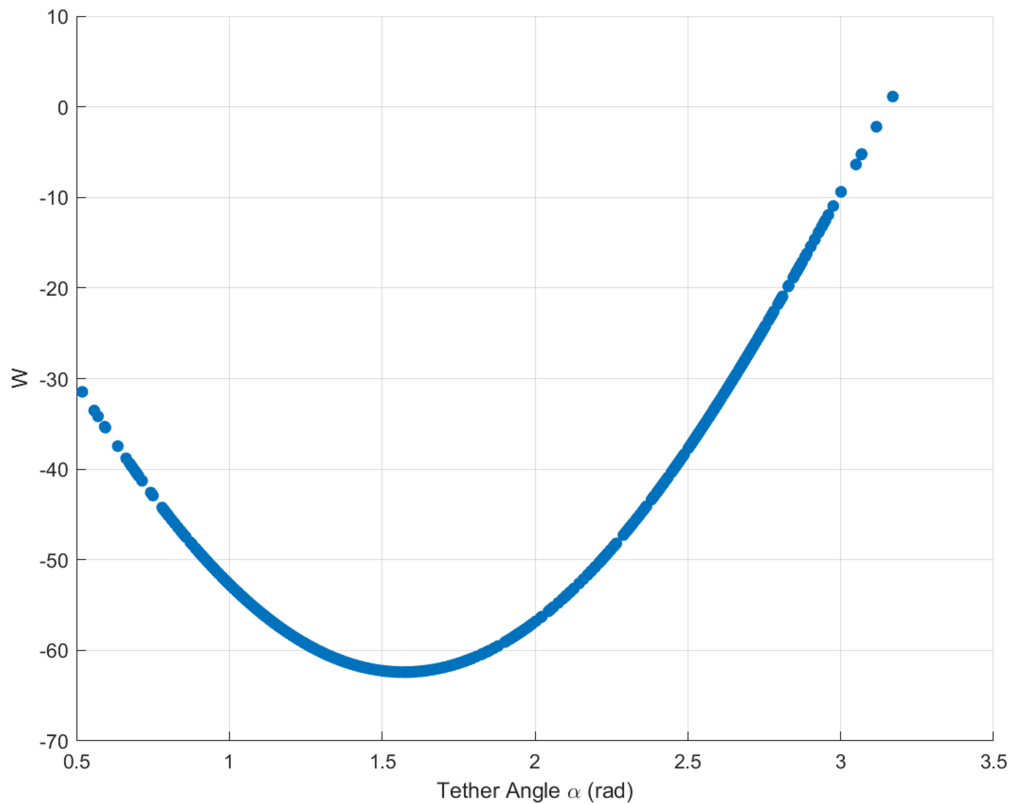


Figure 3.11: Case 3: Local horizontal - important orbital parameters

Figures 3.8 and 3.9 show the effect of increasing thrust in the local vertical initial configuration as compared to the baseline case 1 shown in figure 3.3. The results show that adding any amount of force increases the amplitude of oscillation of the tether from that seen in case 1 (vertical configuration).

The stabilizing effects of forces on unstable configurations have been studied previously [1, 14]. Comparing figure 3.10 to the baseline horizontal case (figure 3.4) it is observed that by applying even a small amount force, the initially unstable system becomes oscillatory. For both cases 2 and 3, amplitude of oscillation is high for engineering applications, reaching values above a half-rotation.



**Figure 3.12:** Case 3: Local horizontal - non-dimensional potential energy vs tether angle

In figure 3.12 the non-dimensional potential energy is plotted against tether angle for case 3 in local horizontal. Figure 3.12 shows a stable point located around local horizontal ( $\alpha \approx 1.67$  radians). The potential energy in this case is shifted towards higher tether an-

gles, reflecting the same tether angle behaviour seen in figure 3.11 wherein the amplitude of tether angle is relatively high.

Despite the high amplitudes of oscillation in both cases 2 and 3 in both initial configurations, as time progresses, the amplitude of oscillation decreases. This trend is particularly apparent in case 3 with a larger magnitude of applied thrust. As well, both configurations in cases 2 and 3 show an increasing orbital radius which decreases the potential energy of the system. Concurrently, with the applied force on the system, kinetic energy as well as overall energy in the system increases.

## 3.4 Effect of Aerodynamics

In this section the effects of aerodynamic lift and drag are presented. First, the effects of the maximum drag and lift in the design space are observed in the absence of thrust force. Maximum overall force, including thrust, is presented subsequently. Then, thrust is decreased to a moderate amount and the effects of varying aerodynamic lift are evaluated with full drag force. Finally, a special case of the horizontal configuration is presented to show another form the instability of the system takes.

### 3.4.1 Maximum Aerodynamic Force

Case 4 defines the parameters which apply the maximum amount of aerodynamic force to the system within the defined design space in the absence of applied thrust. From these initial conditions, as well as equations 2.19 and 2.20 the magnitude aerodynamic forces acting on the system can be calculated simply by taking the magnitude of the above force vectors at every time-step. Figure 3.13 shows the plotted drag force (left) and lift force (right) over time for case 4 initial vertical configuration. The oscillatory and increasing values loosely follow the trends in decreasing orbital radius. These trends are due to changes in density as well as changes in velocity. Based on the chosen density model density increases with decreasing radius  $R_T$ , increasing aerodynamic forces. Further-

more, lower orbits require a higher orbital rate to maintain, increasing the velocity of the debris, increasing aerodynamic forces.

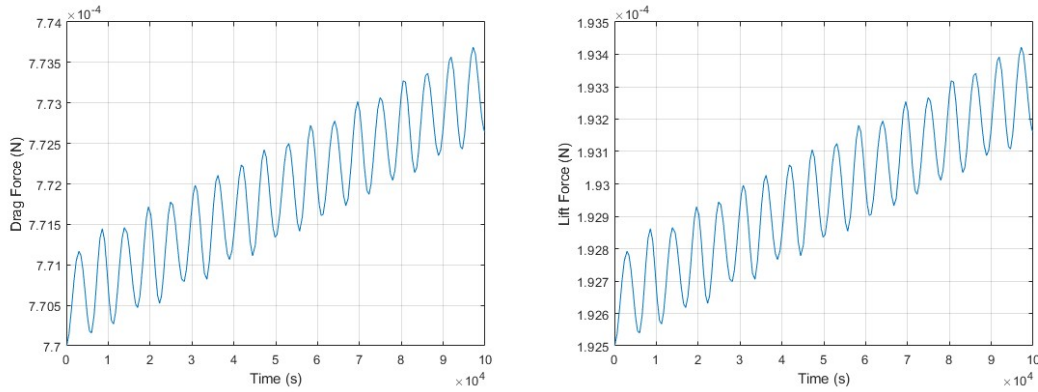


**Figure 3.13:** Case 4: Local vertical - magnitude of applied aerodynamic forces

Overall, figures 3.15 and 3.16 show similar overall trends to their baseline counterparts in figures 3.3 and 3.4. In this case, figure 3.15 shows stable oscillation in tether angle and figure 3.16 shows unstable rotations in tether angle.

With the maximum aerodynamic forces within this design space, forces are not high enough to fully stabilize or destabilize the system.

In the near local vertical configuration, aerodynamic forces shift the oscillations in tether angle clockwise, ultimately decreasing the amplitude of oscillation over time. In the near local horizontal configuration, over the same time-span as case 1, we see that the decrease in tether angle is much more gradual. In both these case, aerodynamic forces have a similar stabilizing effect as seen by thrust force previously in literature [1, 14] and section 3.3 as well as to be presented in section 3.5.

Figure 3.14 presents the oscillation in debris angle for the local vertical configuration of case 4. Similar results were obtained for local horizontal. In this case, we see a stark difference from the behaviour seen in figures 3.6 or 3.5 from case 1. In figure 3.14, the debris oscillates uniformly about a value of roughly  $\phi = 1.75$  with a relatively large amplitude. This behaviour is not the primary focus of this these but could also pose a danger to engineering systems. Conversely, the behaviour in case 1 show either consistent increasing or

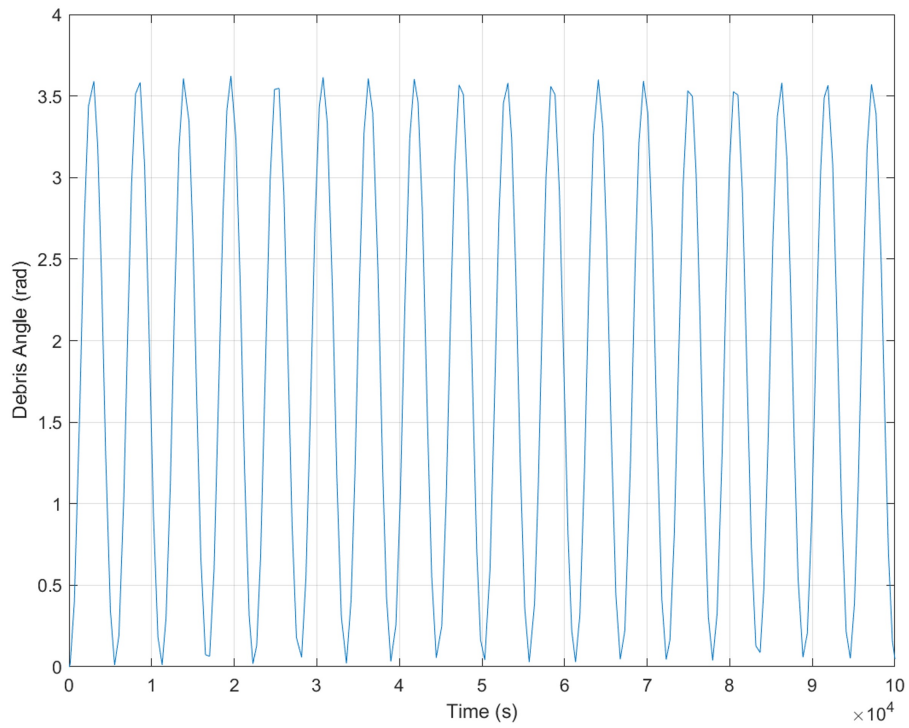


**Figure 3.14:** Case 4: Local vertical - behaviour of debris angle

decreasing trends in debris angle. The behaviour seen in figure 3.14 for case 4 could be a result of the oscillations in tether angle changing the angle at which aerodynamic lift and drag are applied. This oscillatory pattern, combined with the oscillation in radius and impact of changing density and velocity, contribute to the periodicity seen debris angle in the presence of strong aerodynamic forces.

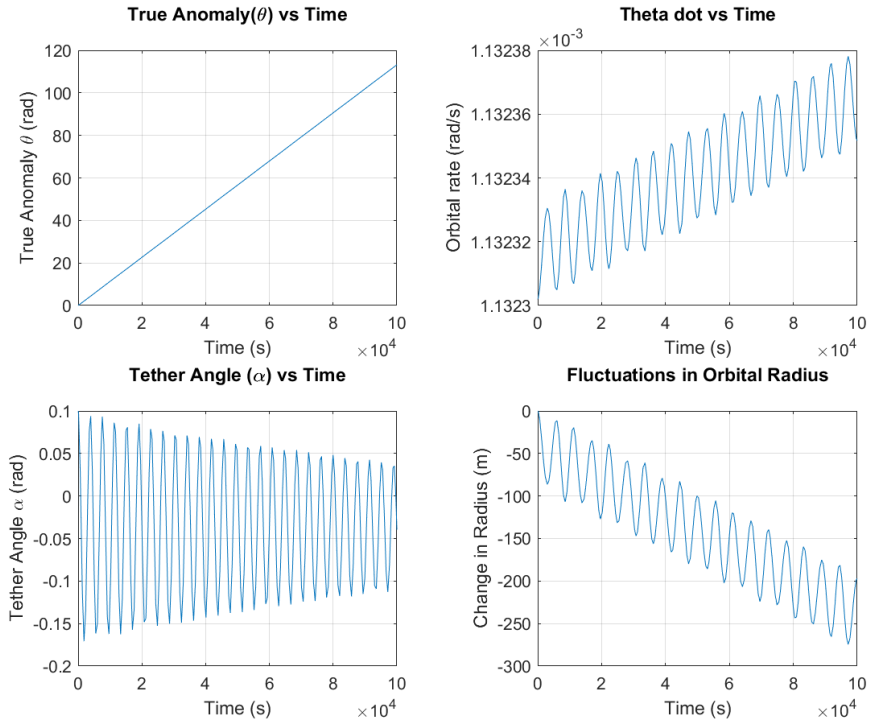


Figure 3.15: Case 4: Local vertical - important orbital parameters

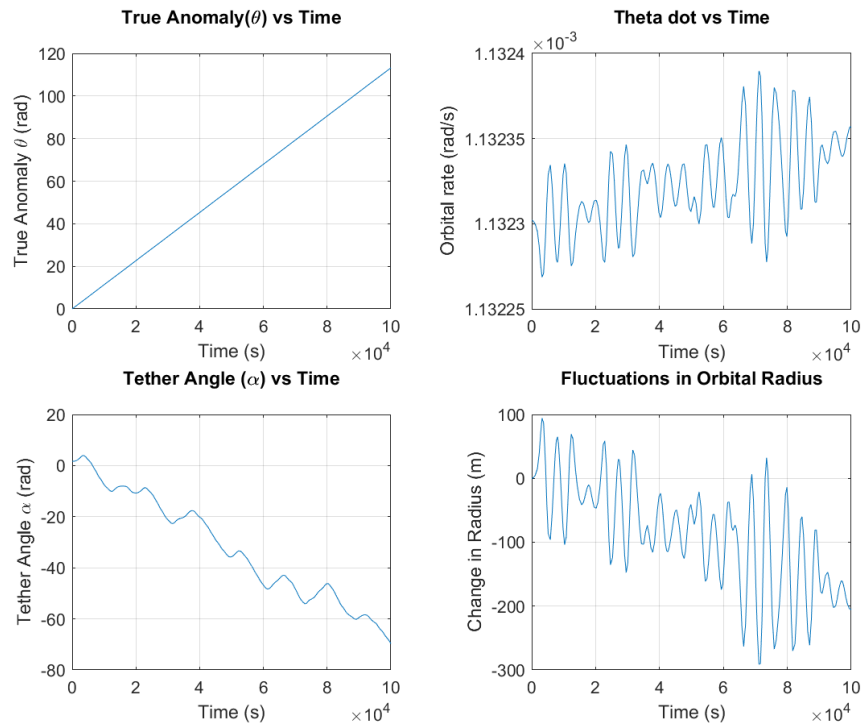


Figure 3.16: Case 4: Local horizontal - important orbital parameters

### 3.4.2 Maximum Overall Force

Case 5 defines the parameters which apply the maximum amount of overall force to the system within the defined design space.

Figures 3.17 and 3.18 show the results of case 5 for initial conditions near local vertical and near local horizontal, respectively. In these results we see similar trends to those seen in case 2 such as the increasing effect of aerodynamic force on initial oscillation amplitude. As well, over time, we see the amplitude in oscillation in tether angle decrease in both configurations, tending towards a more maintainable, stable behaviour. As well, these cases show similar equilibrium points, wherein oscillations occur about an equilibrium position of local horizontal from both initial tether configurations.

It should be noted that the results with aerodynamic forces contain much more fluctuations than those with only thrust force. This result is consistent among the conducted tests. Aerodynamic forces depend on many variables within the dynamic system, leading to more fluctuations in the solution over time. Changes and oscillations in any of the generalized coordinates are liable to change the magnitude of aerodynamic force either through varying air density or varying debris velocity.

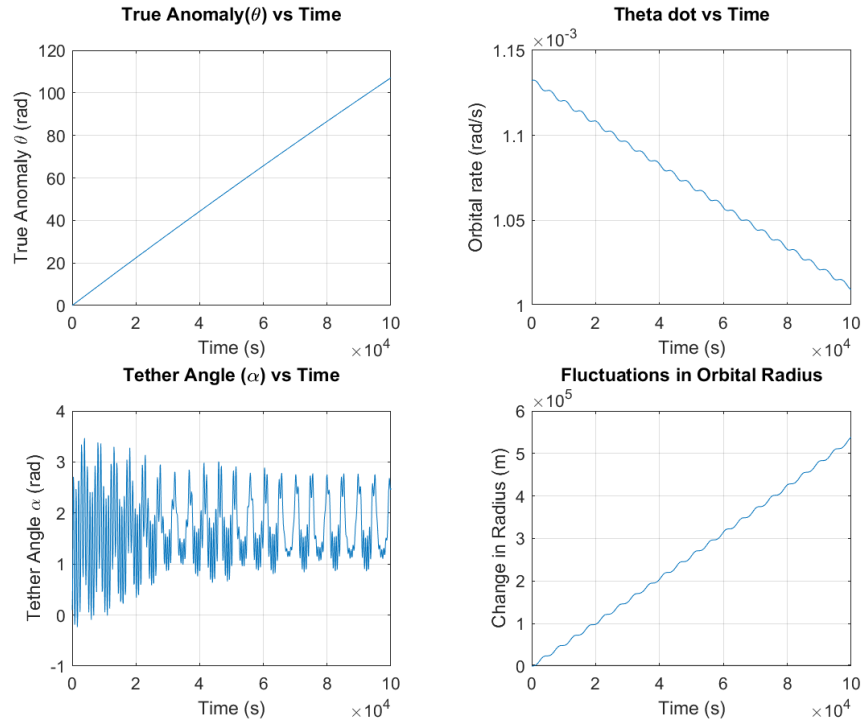


**Figure 3.17:** Case 5: Local vertical - important orbital parameters

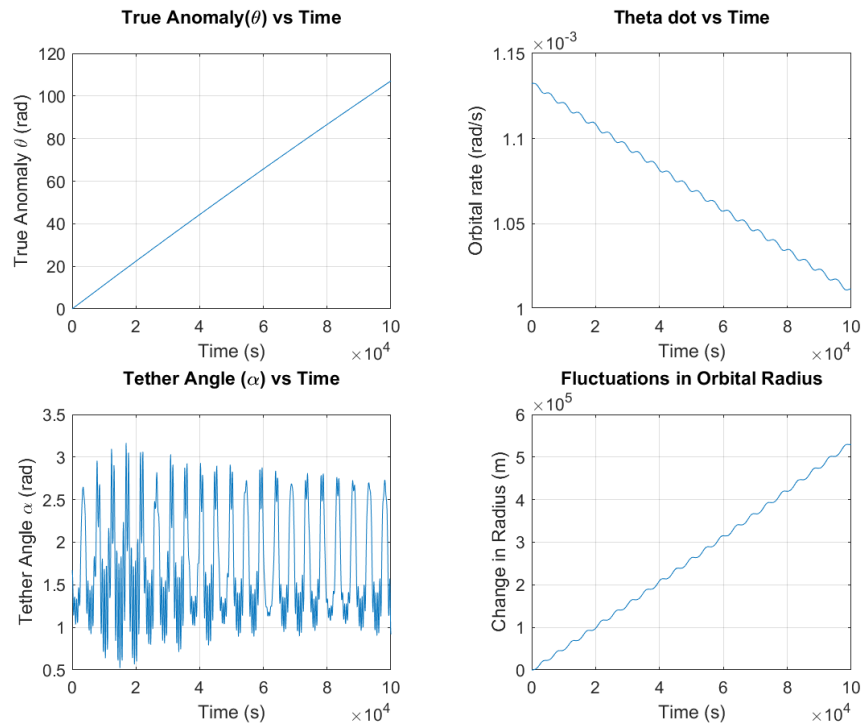


**Figure 3.18:** Case 5: Local horizontal - important orbital parameters

### 3.4.3 Aerodynamics with Increasing Lift

Cases 6 and 7 present scenarios with moderate thrust for increasing lift coefficient within the bounds of the design space. Figures 3.19 and 3.20 show the results for case 6 from initial near local vertical and near local horizontal. Similarly, results for case 7 are presented in appendix A.2. Results for case 6 and case 7 were very similar as a result of such a narrow design space. In reality, the choice of lift coefficients reflect an accurate span as lift coefficients do not tend to vary significantly for common object shapes. As a result, cases 6 and 7 visually appear similar to case 5 in section 3.4.2, leading to the conclusion that lift has very little impact on system stability in space debris towing systems.

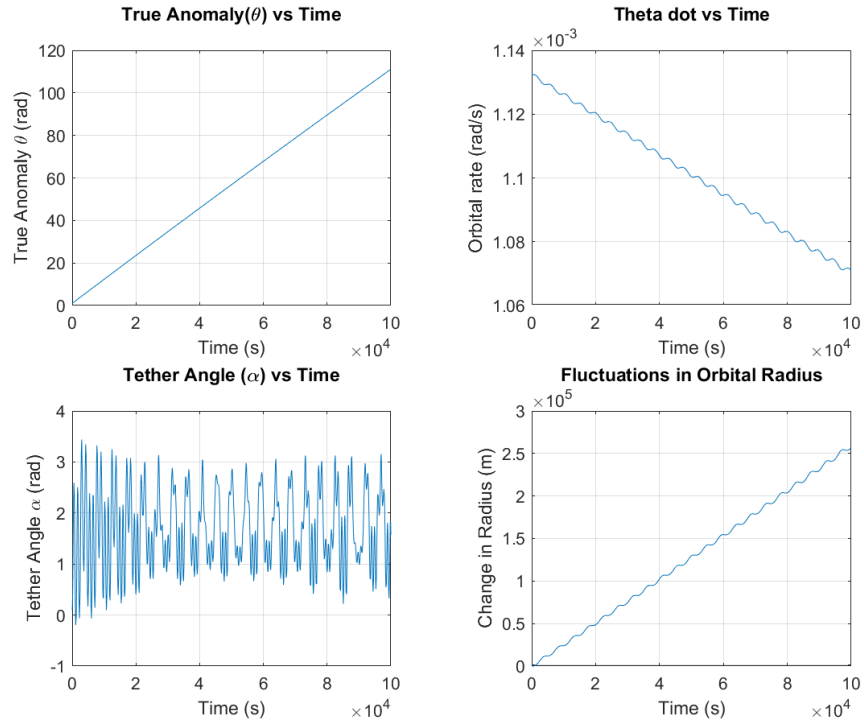


**Figure 3.19:** Case 6: Local vertical - important orbital parameters

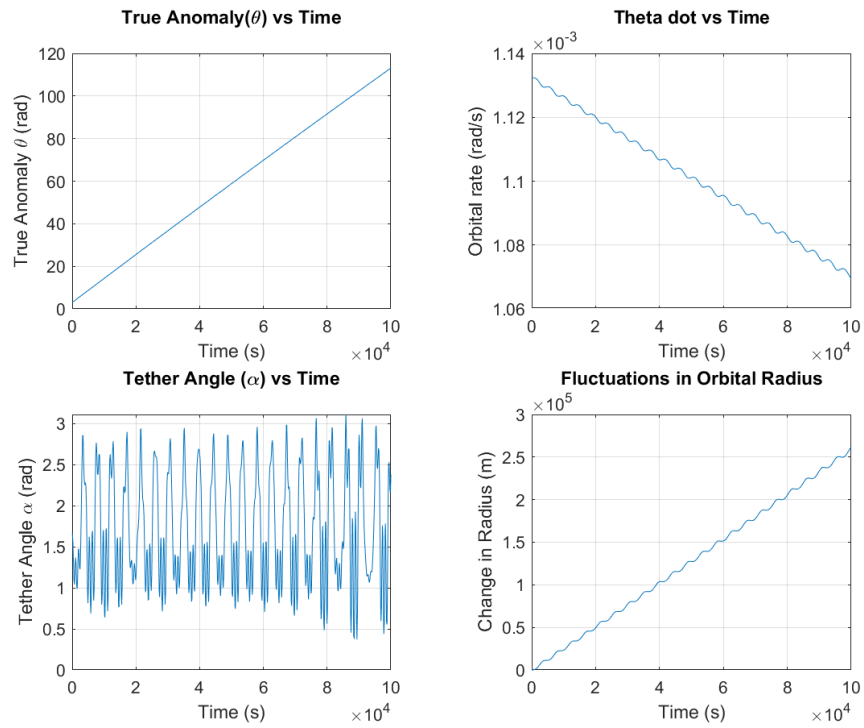


**Figure 3.20:** Case 6: Local horizontal - important orbital parameters

### 3.4.4 Shifting Equilibrium

Case 8 is one set of conditions which produced particularly interesting results from an initial local horizontal configuration. Figure 3.21 shows the behaviour of case 8 over an extended time frame. In this simulation, we see the tether switch between several equilibria. Oscillations about these equilibria were typical for simulations conducted with aerodynamic forces and thrust as observed in previous cases (around 1.5 radians). Although large oscillation amplitude remains a problem in systems with applied external forces, case 8 provides an interesting example in the non-linear dynamics of the tether tug system.

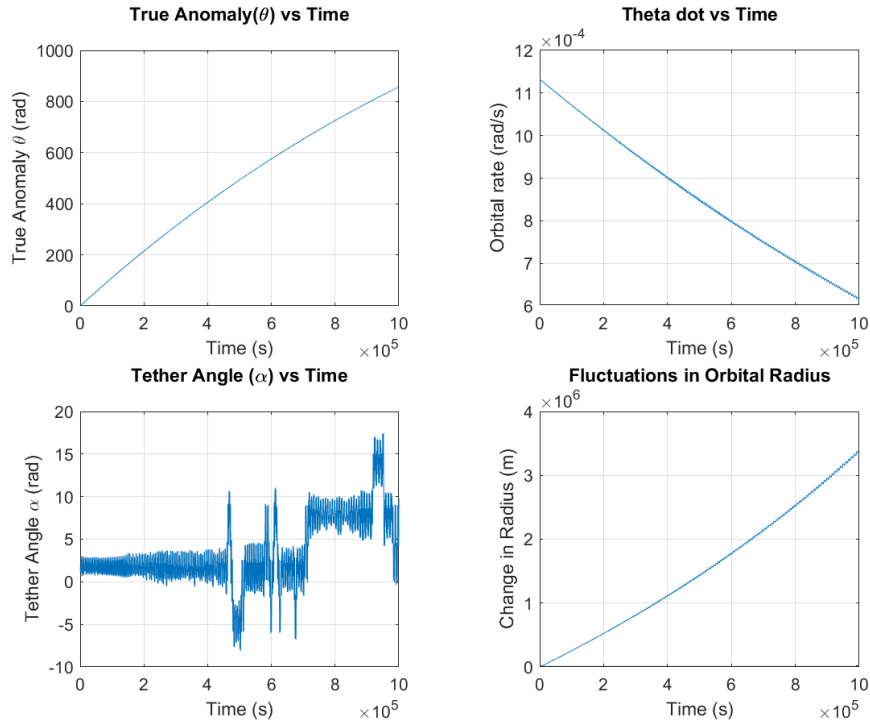


**Figure 3.21:** Case 8: Local horizontal - important orbital parameters

Figure 3.22 shows the plotted non-dimensional potential energy of the system. In this figure, one can observe several maxima and several minima, marking the stable and unstable equilibria of the system as discussed in section 3.2 regarding equation 3.3. Comparing the equilibrium qualitatively between the plot of tether angle in figure 3.21 and

the local minima in figure 3.22, one can clearly draw connections between the behaviour of the two plots.

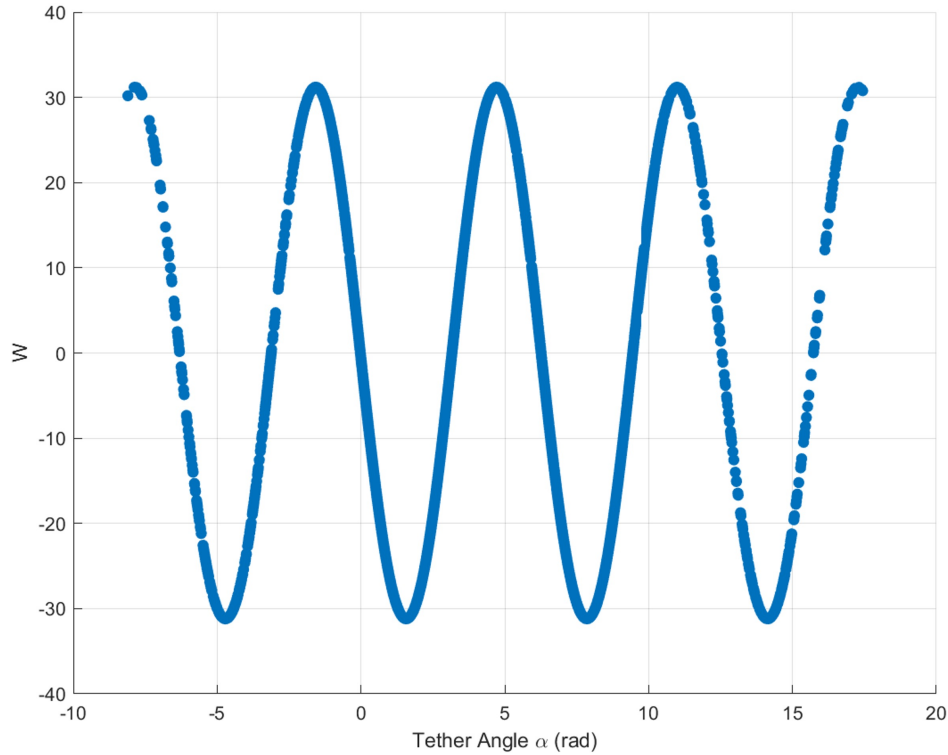


**Figure 3.22:** Case 8: Local horizontal - non-dimensional potential energy

### 3.5 Stabilization with Force

In this section, case 9 is presented. With an increased amount of thrust force over an extended time-frame, the stabilizing effect of applied thrust force is clearly illustrated as expected from literature [1, 14]. Several example tests were conducted which illustrated this result with varying aerodynamic forces, all producing the same trends in stabilizing behaviour, albeit within different speeds of stabilization.

The trend is that increasing the magnitude of force, increases the speed of stabilization. Ultimately, oscillation amplitude decreases to values around 0.1 radians from local horizontal in the local vertical configuration case at the end of 1,000,000 s as shown here

in figure 3.23. For the near local horizontal case, stability is slower to progress, reaching an oscillation amplitude of about 0.15 radians. In either case, the end results are stable oscillations about the local horizontal position with reasonable amplitude, offering promise for future applications. For the design space used in this thesis, the thrust values were too low to stabilize the system within a time-span useful for active debris removal.

With increasing force on the system, stability is approached more rapidly, offering hope to the concept of designing satellites with high lift and drag coefficients at the time of decommission. With fuel-savings in mind, increasing aerodynamic force suitably at this time in the satellite's lifespan could reduce the amount of thrust needed to reach stability to safely de-orbit non-functional space debris.

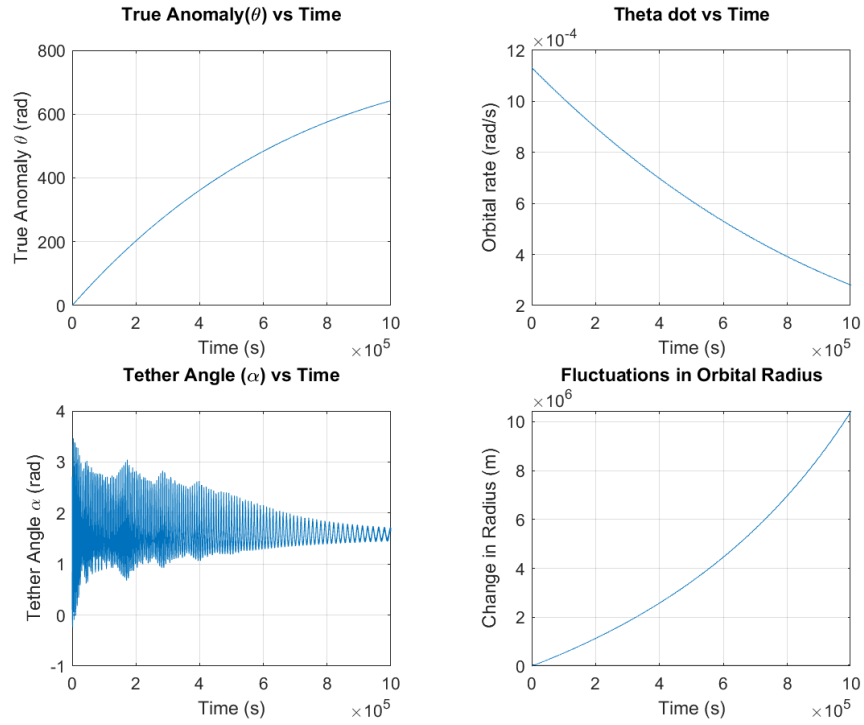


Figure 3.23: Case 9: Local vertical - important orbital parameters

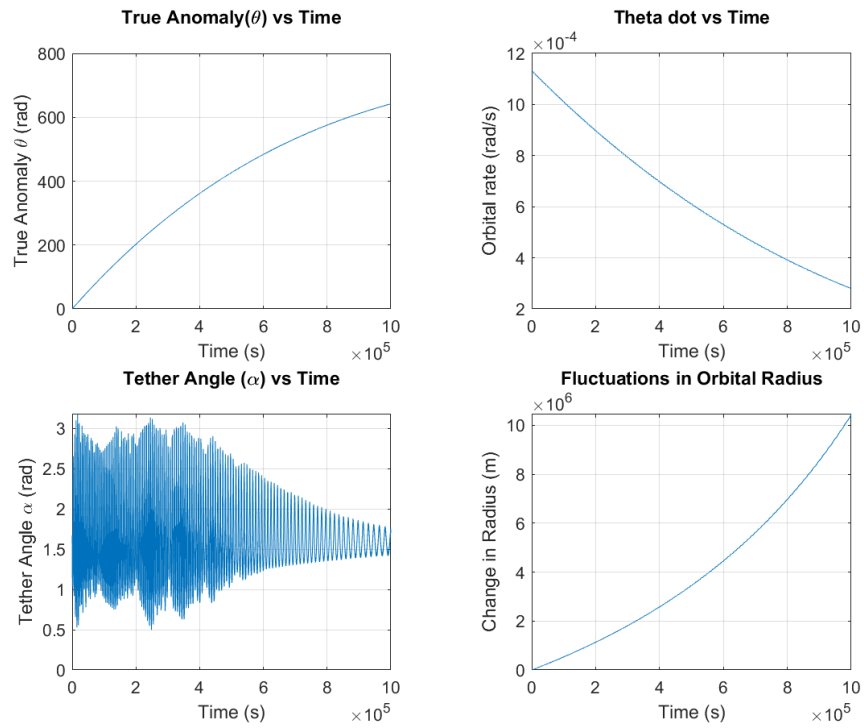


Figure 3.24: Case 9: Local horizontal - important orbital parameters

## 3.6 Discussion

In this chapter, numerical simulation is presented for nine key test cases. An example of validation through work-energy theorem, as well as conservation of energy, is shown; lending credibility to the results discussed here-within.

Building on previous work [1, 2, 13, 14], preliminary results showed the expected behaviour of tethered systems in free oscillation from near local vertical and near local horizontal initial conditions. Namely, stable behaviour was observed for systems beginning near local vertical and unstable behaviour was observed for systems beginning near local horizontal.

Subsequently, a study was conducted to demonstrate the effects of applied forces thrust, aerodynamic drag, and aerodynamic lift on the tethered system. The behaviour of the tether (chiefly tether angle  $\alpha$  was of key interest in analysis). As well, non-dimensional potential energy  $W$  whose formula is derived from literature [3] is used to examine equilibrium point behaviour.

In case 4, the effects of aerodynamic forces are apparently negligible. With very small calculated force values it is understandable in the context of this simulation that case 4 should not differ significantly from case 1 (free oscillation). This is thought to be a limitation of the selected design space. Although realistic for typical objects, a more design-oriented approach may consider taking a less nominal range of coefficients; with the intention of designing systems to fit these debris properties.

Initially, it appears applying force to the system increases the amplitude of oscillation of the tether. In these cases, this behaviour was explained as a result of changing energy in the system, either by adding energy due to thrust or initially pushing the tether to a new equilibrium point.

Overall, stability in the oscillation in tether angle can be seen to stabilize with increasing amounts of applied force. Previously, thrust has been examined as a stabilizing

mechanism [1, 14]. Here, it is suggested that aerodynamic properties may be used in decommission to apply more force to the system without expending more fuel.

The most common equilibrium point throughout simulation tended to local horizontal, even in cases of initial configurations near local vertical. This behaviour was suspected to be a result of a perceived moment applied between the thrust force and aerodynamic drag. This couple moment is thought to rotate the tether preferentially into horizontal configuration, parallel to the direction of applied force in most shown configurations.

Finally, oscillation in of the debris is considered negligible in most test cases. However, stable oscillation of the debris can be seen in case 4. This behaviour is analysed in section 3.4.1 with reference to the combined oscillatory effects of the orbital elements of the system and the tether, as well as the influence of debris velocity as well as the effect of orbital radius on air density.

# Chapter 4

## Conclusion

Satellite and space-based technologies are an important part of the modern world as research and exploration expands beyond Earth's atmosphere. The escalating challenge of space debris in lower Earth orbit (LEO) necessitates effective mitigation strategies, with active space debris removal using tether-based systems emerging as a promising and cost-effective solution.

This thesis presents a numerical simulation of the dynamics of the tethered tug-debris system in four dimensions. Using a Lagrangian approach, the equations of motion are derived within the reference frame of the space tug. As well, an exponential model is used for air density in lower Earth orbits.

This work places emphasis on the effect of aerodynamic drag present in low earth orbit on the stability of the tethered system, exploring a historically understudied facet of this complex system. By implementing these equations into a numerical program in MATLAB, numerical simulation is conducted to explore a range of scenarios. The dynamics of the tug-tether-debris system are analyzed, emphasizing the nonlinear nature and potential instability of such systems.

Throughout analysis, focus is placed on the behaviour of equilibrium points, tether oscillations, and the effectiveness of stabilization methods. Key parameters such as the

aerodynamic properties of debris, tether orientation, and thrust magnitude and direction are thoroughly investigated within a realistic design space.

This thesis replicates results seen in previous research as to the stability of local vertical configurations and the instability of local horizontal configurations. Furthermore, the stabilizing effects of applied force on tethered satellite systems is expanded, suggesting fuel-saving methods by designing systems with aerodynamic properties conducive to stable towing configurations.

This work strives to contribute to the fundamental knowledge of tethered satellite systems and introduce novel insights into the impact of aerodynamics on the stability of space debris towing systems. Modeling the system in the frame of the space tug facilitates practical applications in control system design, enabling more effective tracking and implementation. As we strive to enhance space debris removal systems, control mechanisms, mission planning, and end-of-life satellite design, the findings presented in this study lay the groundwork for future aerospace design.

# Bibliography

- [1] ASLANOV, V., MISRA, A. K., AND YUDINTSEV, V. Chaotic motions of tethered satellites with low thrust. In *67th International Astronautical Congress (IAC), Guadalajara, Mexico* (2016).
- [2] ASLANOV, V., AND YUDINTSEV, V. Dynamics of large space debris removal using tethered space tug. *Acta Astronautica* 91 (2013), 149–156.
- [3] ASLANOV, V. S., MISRA, A. K., AND YUDINTSEV, V. V. Chaotic attitude motion of a low-thrust tug-debris tethered system in a keplerian orbit. *Acta astronautica* 139 (2017), 419–427.
- [4] BONNAL, C. Space debris in a nutshell: Status and ways forward. In *3rd International Conference on Space Situational Awareness (ICSSA 2022), Madrid, Spain* (2022).
- [5] EUROPEAN SPACE AGENCY. ATV: A Very Special Delivery - Lesson Notes.
- [6] EUROPEAN SPACE AGENCY. Hypervelocity impact sample, 2009.
- [7] JASPER, L., AND SCHAUB, H. Tethered towing using open-loop input-shaping and discrete thrust levels. *Acta Astronautica* 105, 1 (2014), 373–384.
- [8] KELSO, T., ET AL. Analysis of the iridium 33-cosmos 2251 collision. *Advances in the Astronautical Sciences* 135, 2 (2009), 1099–1112.

- [9] KESSLER, D. J., AND COUR-PALAIS, B. G. Collision frequency of artificial satellites: The creation of a debris belt. *Journal of Geophysical Research: Space Physics* 83, A6 (1978), 2637–2646.
- [10] MARK, C. P., AND KAMATH, S. Review of active space debris removal methods. *Space Policy* 47 (2019), 194–206.
- [11] MATHWORKS. Matlab documentation, Year.
- [12] MEHDI, K., AND MISRA ARUN, K. Effects of aerodynamic lift on the stability of tethered subsatellite system. *ISSN 0065-3438* (1993), 1263–1281.
- [13] MISRA, A. K. Debris removal using a space tug. In *3rd International Conference on Space Situational Awareness (ICSSA 2022), Madrid, Spain* (2022).
- [14] MISRA, A. K., SAYNAK, R., AND DOSS, A. P. Towing of space debris using a tether. In *68th International Astronautical Congress (IAC), Adelaide, Australia* (2017).
- [15] OF MECHANICAL ENGINEERS, I. ‘space tether’ could de-orbit space junk without using propellant, 2022.
- [16] PARDINI, C., AND ANSELMO, L. Evaluating the impact of space activities in low earth orbit. *Acta Astronautica* 184 (2021), 11–22.
- [17] PEARSON, J., LEVIN, E., OLDSON, J., AND WYKES, H. Lunar space elevators for cislunar space development. Retrieved from NASA Institute for Advanced Concepts: [http://www.niac.usra.edu/files/studies/final\\_report/1032Pearson.pdf](http://www.niac.usra.edu/files/studies/final_report/1032Pearson.pdf) (2005).
- [18] PHIPPS, C. R. L adroit—a spaceborne ultraviolet laser system for space debris clearing. *Acta Astronautica* 104, 1 (2014), 243–255.
- [19] QI, R., MISRA, A. K., AND ZUO, Z. Active debris removal using double-tethered space-tug system. *Journal of Guidance, Control, and Dynamics* 40, 3 (2017), 722–730.

- [20] SGOBBA, T., AND RONGIER, I. *Space Safety is No Accident: The 7th IAASS Conference*. Springer, 2015.

# Appendices

# Appendix A

## Additional Plots

### A.1 Preliminary Results: Conservation of Energy

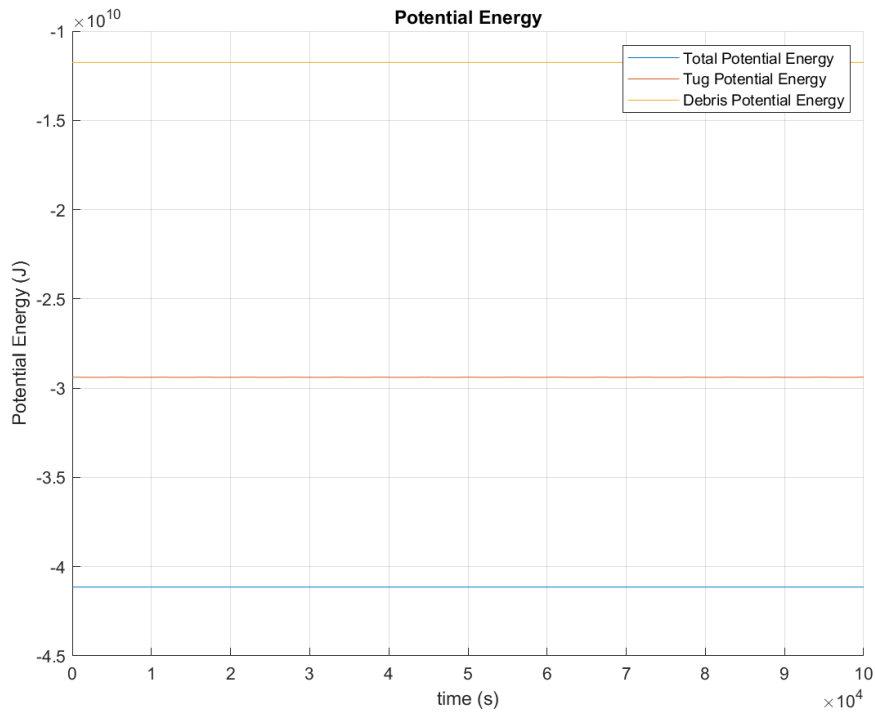


Figure A.1: Potential Energy vs Time from Local Vertical in Free Oscillation (Case 1)

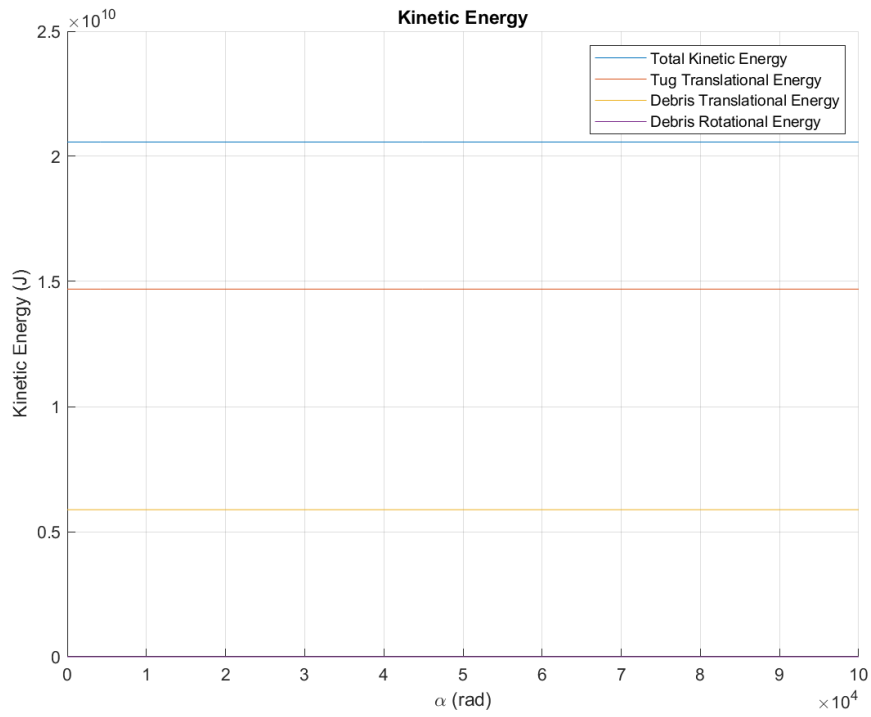


Figure A.2: Kinetic Energy vs Time from Local Vertical in Free Oscillation (Case 1)

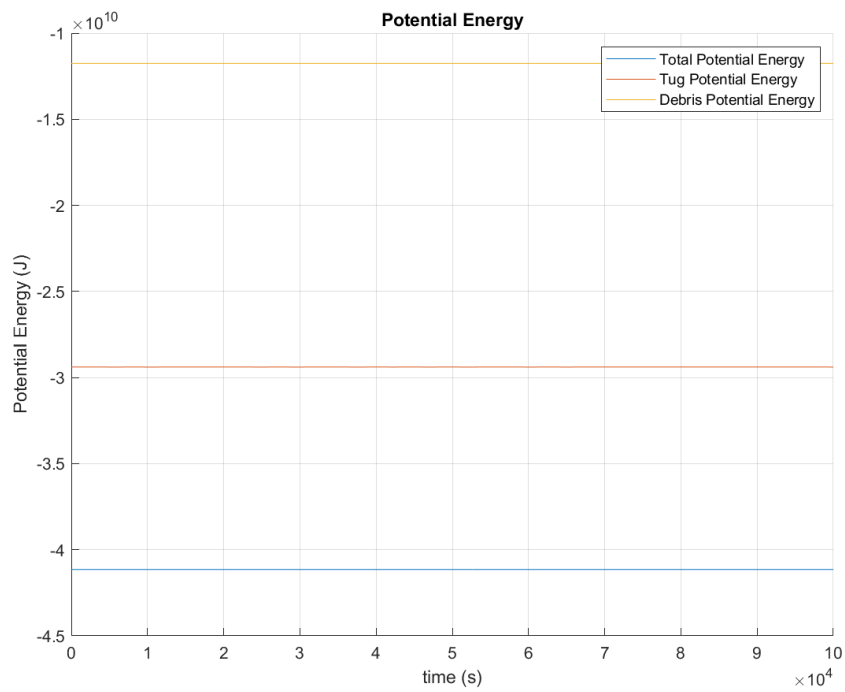
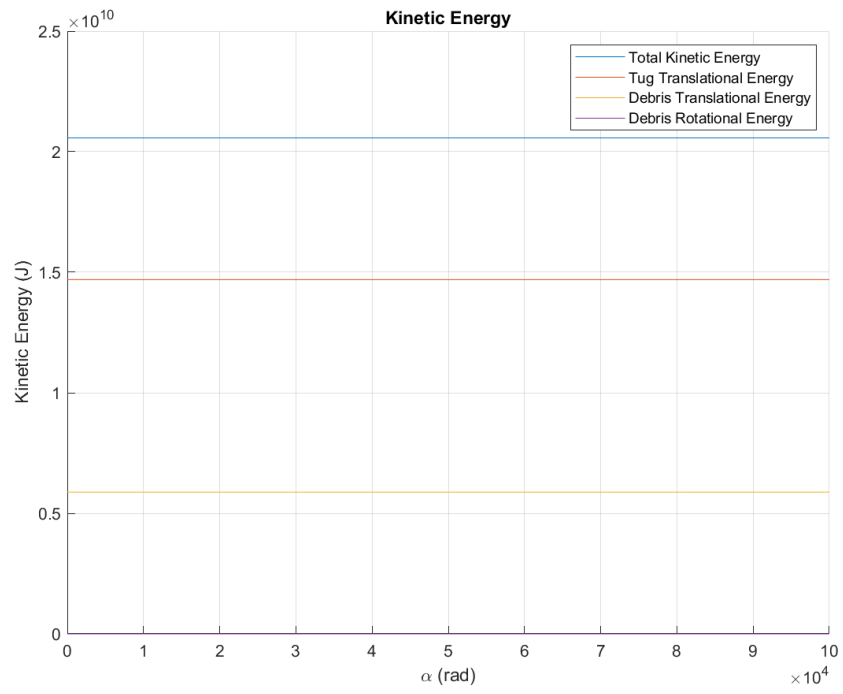


Figure A.3: Potential Energy vs Time from Local Horizontal in Free Oscillation (Case 1)



**Figure A.4:** Kinetic Energy vs Time from Local Horizontal in Free Oscillation (Case 1)

## A.2 Case 7: Effects of Aerodynamics

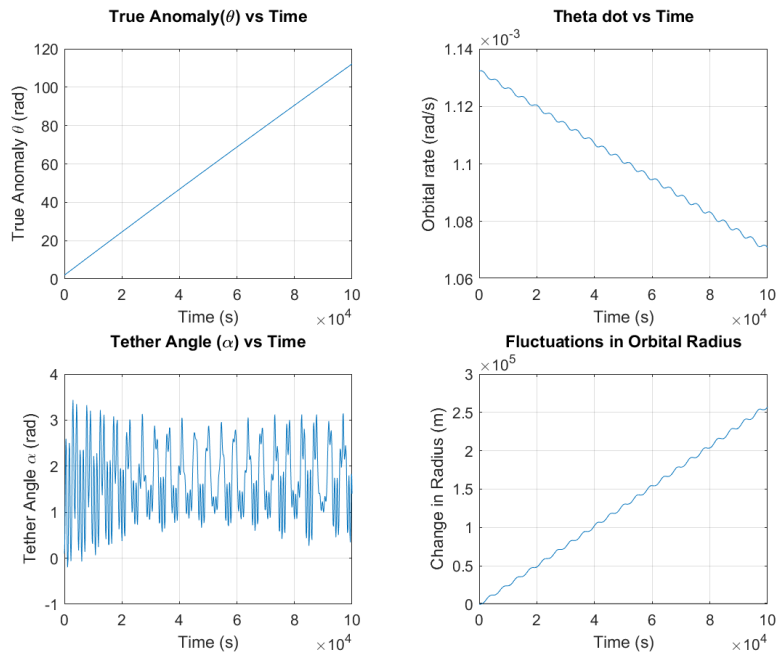


Figure A.5: Case 7: Local vertical - important orbital parameters

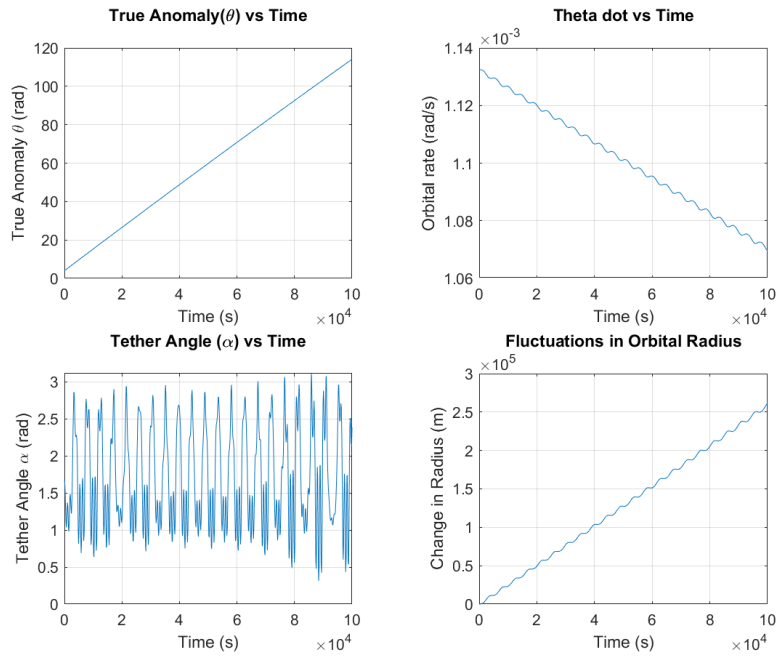


Figure A.6: Case 7: Local horizontal - important orbital parameters

# Appendix B

## MATLAB Code

```
1 tic
2 input = readtable("Testing Plans.xlsx",'Sheet', 2 , 'Range', 'D5:T26');
3 for i= 1:length(input{1,:})
4     folder_name=''; F=0; beta_degrees=0; C_D=0;
5     C_L=0; area=0; l=0; d=0; m_T=0; m_D=0;
6     I_G=0; R0=0; M0=0; A0=0; p0=0; dR0=0;
7     dA0=0; dp0=0; timespan=[];
8
9     column = input(:,i);
10    [folder_name, F, beta_degrees, C_D, C_L, area, l, d, m_T, m_D, I_G,
11     R0, M0, dM0, A0, p0, dR0, dA0, dp0, timespan] = myread_excel(
12     column);
13
14    %Constants
15    mu= 3.98*10^14;           %Standard gravitational parameter for
16     Earth (m^3/s^2)
17
18    R_E= 6371*10^3;          %Radius of the Earth (m)
```

```

17
18 %Adjustments
19 beta= beta_degrees*pi/180;          %angle of applied thrust (radians)
20
21 system_0s = [A0 dA0 R0 dR0 M0 dM0 p0 dp0];
22
23 reference= 6771000;
24 rho_0 = 2.62*10^(-12);          % Density of air (kg/m^3)
25 H_0 = 58200;                    % Scale height (from Paper "Effects of
    Aerodynamic Lift on the Stability of Tethered Satellite Systems
    " )
26
27 %symbolic stuff
28 rho = rho_0*exp(-(R-reference)/H_0);
29
30 v_d = sqrt(diff(R)^2+2*diff(R)*l*(diff(A)+diff(M))*sin(A)+l^2*(diff
    (A)+diff(M))^2+diff(M)^2*R^2-2*l*diff(M)*R*(diff(A)+diff(M))*cos
    (A)) ;
31
32 Q_R= -F*sin(beta)+C_L*area*rho/2*v_d*(diff(M)*R-l*(diff(A)+diff(M))
    *cos(A))-C_D*area*rho/2*v_d*(diff(R)+l*(diff(A)+diff(M))*sin(A))
    ;
33 Q_M= F*R*cos(beta)+v_d*area*rho/2*(C_L*(-l*diff(M)*R*sin(A)-l*diff(
    R)*cos(A)-R*diff(R)-l*R*(diff(A)+diff(M))*sin(A))+C_D*(l*diff(R)
    *sin(A)+l^2*(diff(A)+diff(M))-l*diff(M)*R*cos(A)-diff(M)*R^2+R*l
    *(diff(A)+diff(M))*cos(A));
34 Q_A= v_d*l*area*rho/2*(C_L*diff(M)*R*sin(A)+C_D*diff(R)*sin(A)-C_L*
    diff(R)*cos(A)-C_D*diff(M)*R*cos(A)+C_D*l*(diff(A)+diff(M)));

```

```

35 Q_p= v_d*d*area*rho/2*(C_L*diff(M)*R*sin(p)+C_L*l*(diff(A)+diff(M))
    *sin(A-p)-C_D*diff(R)*sin(p)-C_D*l*(diff(A)+diff(M))*cos(A+p)+
    C_L*diff(R)*cos(p)+C_D*diff(M)*R*cos(p));
36
37 %Lagrangian Equations
38 R_T = m_T*diff(R,2) + m_D*(diff(R,2) + l*(diff(A,2) + diff(M,2))*sin
    (A) + diff(A)*l*(diff(A)+diff(M))*cos(A) - m_T*diff(M)^2*R -
    m_D*(diff(M)^2*R-l*diff(M)*(diff(A)+diff(M))*cos(A)) + mu*(m_T/(R
    ^2)+m_D*(R-l*cos(A))/(R^2-2*R*l*cos(A)+l^2)^(3/2)) == Q_R;
39 theta = m_T*diff(M,2)*R^2 + 2*m_T*diff(M)*R*diff(R) + m_D*(diff(R
    ,2)*l*sin(A) + diff(R)*diff(A)*l*cos(A) + l^2*(diff(A,2)+diff(M
    ,2)) + diff(M,2)*R^2 + 2*diff(M)*R*diff(R) - l*diff(R)*diff(M)*
    cos(A) - l*R*diff(M,2)*cos(A) + l*diff(A)*R*diff(M)*sin(A) +
    I_G*(diff(p,2) + diff(M,2)) == Q_M;
40 alpha = m_D*(diff(R,2)*l*sin(A) + diff(A)*diff(R)*l*cos(A) + l^2*(
    diff(A,2)+diff(M,2)) - l*diff(M,2)*R*cos(A) - l*diff(M)*diff(R)*
    cos(A) + l*diff(A)*diff(M)*R*sin(A) - diff(R)*l*(diff(A)+diff(M)
    )*cos(A) - l*diff(M)*R*(diff(A)+diff(M))*sin(A) + mu*R*l*sin(A)
    /(R^2-2*R*l*cos(A)+l^2)^(3/2)) == Q_A;
41 phi = I_G*(diff(p,2) + diff(M,2)) == Q_p;
42
43 [system, variables]= odeToVectorField(R_T, theta, alpha, phi);
44 statespace= matlabFunction(system, 'vars', {'t', 'Y'});
45
46 % disp(variables)
47
48 sol= ode45(statespace, timespan, system_0s);
49
50 alpha_data = sol.y(1,:);
51 alphasdot_data = sol.y(2,:);

```

```

52 R_data = sol.y(3,:);
53 dR_data = sol.y(4,:);
54 theta_data = sol.y(5,:);
55 thetadot_data = sol.y(6,:);
56 phi_data = sol.y(7,:);
57 phidot_data = sol.y(8,:);
58
59 tug_vel = sqrt(dR_data.^2+thetadot_data.^2.*R_data.^2);
60
61 debris_vel = sqrt(dR_data.^2+2.*dR_data.*l.*(alpha_data+theta_data)
    .*sin(alpha_data)+l.^2.*(alpha_data+theta_data).^2+theta_data
    .^2.*R_data.^2-2.*l.*theta_data.*R_data.*(alpha_data+theta_data)
    .*cos(alpha_data)) ;
62 F_drag = C_D.*area.*rho_0.*exp(-(R_data-reference)./H_0)./2.*
    debris_vel.^2;
63 F_lift = C_L.*area.*rho_0.*exp(-(R_data-reference)./H_0)./2.*
    debris_vel.^2;
64
65 properties = [l, d, m_T, m_D, I_G, F, F_drag, F_lift, debris_vel,
    tug_vel];
66 data= [[sol.x]; [R_data]; [dR_data]; [theta_data]; [thetadot_data];
    [alpha_data]; [alphadot_data]; [phi_data]; [phidot_data]];
67 initial_conditions = [R0, M0, A0, p0, dR0, dM0, dA0, dp0];
68
69 plot_function(folder_name, data, initial_conditions, properties)
70 end
71
72 total_time = toc;
73 disp(strcat("total time elapsed:", string(total_time)))
74

```

```

75 %Functions
76 %returns the megnitude (or length) of the given vecor v
77 function len=magnitude(v)
78     len= sqrt(v(1)^2 + v(2)^2 + v(3)^2);
79 end
80
81 %returns a vector normal to the given 2D vecor v
82 function norm=normal2D(v)
83     norm= magnitude(v)*[v(2), v(1), 0];
84 end
85
86 %Density
87 function rho = density(radius)
88     %Reference Density of Air
89     h= radius-6671000;
90     rho_0 = 2.62*10^(-12);           % Density of air (kg/m^3)
91     H_0 = 58200;                   % Scale height (from Paper "Effects of
           Aerodynamic Lift on the Stability of Tethered Satellite Systems
           " )
92     rho = rho_0*exp(-h/H_0);
93     disp(rho)
94 end
95
96 function result = mydot(v, u)
97     result = v(1)*u(1) + v(2)*u(2)+ v(3)*u(3);
98 end

```

**Listing B.1:** Main MATLAB code